CHARGE-SELECTIVE RAMAN SCATTERING AND FLUORESCENCE QUENCHING BY "NANO-METAL ON SEMICONDUCTOR" SUBSTRATES

By

KARTHIK SHANKAR BHATT

Bachelor of Engineering in Mechanical Engineering

Visvesvaraya Technological University

Belgaum, Karnataka, INDIA

2005

Submitted to the Faculty of the
Graduate College of the
Oklahoma State University
in partial fulfillment of
the requirements for
the Degree of
MASTER OF SCIENCE
May, 2010

CHARGE-SELECTIVE RAMAN SCATTERING AND FLUORESCENCE QUENCHING BY "NANO-METAL ON SEMICONDUCTOR SUBSTRATES"

Thesis Approved:

Dr. Kaan Kalkan

Thesis Advisor

Dr. Sandip Harimkar

Dr. Weili Zhang

Dr. A. Gordon Emslie

Dean of the Graduate College

ACKNOWLEDGMENTS

First and foremost, I would like to thank my advisor Dr. Kaan Kalkan for his continuous support and motivation throughout the duration of my Masters program. It would not be possible for me to present this work without his unlimited patience and his knowledge and experience that he imparted to me.

I also acknowledge the time and support given to me by my committee members, Dr. Sandip Harimkar and Dr. Weili Zhang. Furthermore, I would like to thank Dr. Susheng Tan and Terry Colberg from the OSU Microscopy Lab for their immense support and guidance in the fundamentals and working principles of force microscopy and electron microscopy.

The support rendered to me by my colleagues at the Functional Nanomaterials Laboratory has been instrumental in the completion of my thesis. I would especially like to thank Kushagra Singhal for his help in SERS, and Sriharsha Karumuri for his help in UV-Vis spectroscopy.

Finally, I would like to acknowledge my parents Shankar and Raji, my sister Kshama, my brother-in-law Chetan, and Aman for their constant support and unending love, which I relied upon consistently during the course of my graduate studies at OSU.

TABLE OF CONTENTS

Chapter **Page**

I. INTRODUCTION 1

II. BACKGROUND 4

Localized Surface Plasmon Resonance and Hybrid Plasmons 4
Metal on Semiconductor System 8

III. METHODOLOGY 10

Overview 10
Substrate Preparation 11
Nanoparticle Synthesis Using Electroless Deposition 11
Nanoparticle Synthesis Using Vapor Deposition 12
Atomic Force Microscopy 13
Electric Force Microscopy 14
Scanning Electron Microscopy 16
Surface-enhanced Raman Spectroscopy 16
Confocal Laser Scanning Microscopy 17
UV-Vis Spectroscopy 18
Mie-scattering Measurements 19

IV. RESULTS AND DISCUSSION 20

EFM Characterization and Nanoparticle Charging 20
Nanoparticle Size v/s Potential 25
Impact of NP charging: Self-Inhibition of AgNP Growth 29
Impact of NP Charging: Charge-selective Raman Scattering 36
Impact of NP charging: Charge-Selective Fluorescence Quenching 42

Chapter **Page**

V. CONCLUSION.....46

Conclusions.....46
Future Work.....48

REFERENCES.....50

LIST OF FIGURES

Figure **Page**

2.1 Energy band diagram for silver in contact with a p-type semiconductor 8

2.2 Energy band diagram for silver in contact with an n-type semiconductor 9

3.1 Sketch illustrating the electroless reduction of silver nanoparticles on Si 12

3.2 Illustration of the physical vapor deposition process.....13

3.3 Demonstration of laser exposure of analyte and SERS data collection (Courtesy: Dr.Kaan Kalkan).....17

4.1 3D view of an AFM height map of AgNP deposited on p-type Si (a).....21

4.1 3D view of a potential map of AgNP deposited on p-type Si (b).....21

4.2 3D view of an AFM height map of AgNP deposited on n-type Si (a).....23

4.2 3D view of a potential map of AgNP deposited on n-type Si (b).....23

4.3 3D view of an EFM potential map for AuNP synthesized on n-type Si.....24

4.4 Graph illustrating the relation between nanoparticle size and potential for AgNP synthesized on n-type Si (a).....27

4.4 Graph illustrating the relation between nanoparticle size and potential for AgNP synthesized on p-type Si (b).....27

4.5 Episodic capture of the optical extinction spectra of AgNP synthesis on high band gap amorphous Si.....30

4.6 3D waterfall plot of the episodic capture of synthesis of AgNP on high band gap amorphous Si. The relative shifts of the regular and hybrid plasmon peaks are also depicted 31

Figure **Page**

4.7 Schematic of effect of nanoparticle charging on the reduction reaction 33

4.8 AFM height scans of silver nanoparticles synthesized on p-type silicon (a).....34

4.8 AFM height scans of silver nanoparticles synthesized on n-type silicon (b) 34

4.9 Back-scattered measurements showing SPR of AgNP deposited on p-type Si and n-type Si.....35

4.10 SEM micrograph of AgNP vacuum-deposited on n-type silicon (a).....37

4.10 SEM micrograph of AgNP vacuum-deposited on p-type silicon (b).....37

4.11 SERS spectra of fluorescein spotted on p-type silicon and n-type silicon 38

4.12 Sketch of fluorescein molecules getting attracted to (+) AgNP 40

4.13 Sketch of fluorescein molecules getting repelled away from (-) AgNP 40

4.14 SERS spectra of acridine orange spotted on n-type and p-type silicon 41

4.15 Confocal microscopy of 1 µl of fluorescein (1×10^{-7} M) spotted on AgNP deposited on (a) p-type Si, and (b) n-type Si 44

4.15 Confocal microscopy of 1 µl of rhodamine 6G (1×10^{-8} M) spotted on AgNP deposited on (c) p-type Si and (d) n-type Si 44

4.15 Sketch of rhodamine-6G molecules getting attracted to (-) AgNP.....45

4.16 Sketch of rhodamine-6G molecules getting repelled from (+) AgNP 45

CHAPTER I

INTRODUCTION

There has been significant interest generated by noble metal nanoparticles due to the fascinating properties they possess. The earliest and one of the most famous use of noble metal nanoparticles is the Lycurgus cup, discovered in 4th century AD which is ruby red in transmitted light and green in reflected light. Other notable areas where colloidal gold was used in the medieval times include stained glass windows, pottery and other paintings. Their unfading brilliant colors had been a source of mystery until 1857, when Micheal Faraday reported that these intense colors were due to the presence of gold nanoparticles[1], and that the color displayed by these nanoparticles (NP) varied with the NP size. A theoretical solution to this phenomenon was given by Gustav Mie in 1908[2, 3], who accurately solved for the scattering and absorption cross sections of spherical nanoparticles using equations from Maxwell's electromagnetic theory. Subsequently, monolayers of metal nanoparticles have been extensively used in surface plasmon resonance (SPR) sensors[4-6], surface-enhanced Raman scattering (SERS) substrates[7, 8], and other plasmonic devices[9-11]. An interesting attribute of monolayers of metal nanoparticles (NP) synthesized on semiconductor substrates is the selective charging

induced by Fermi level difference. This charging can be tapped in self assembly and the selective adsorption of ions on the NP[12-14]. Typically, NP charging is achieved using surfactant molecules[15-17]. In addition to causing signal interference, surfactants form a physical barrier between analyte and metal, attenuating or completely eliminating surface-enhanced effects.

The present thesis work demonstrates the selective charging of silver nanoparticles (AgNP) synthesized on semiconductor substrates, exploiting the Fermi level differences. Clean, surfactant-free AgNP were synthesized using electroless reduction that involves the synthesis of NP by reduction of the metal salt solution by a semiconductor substrate[18], and vapor deposition[19-22]. EFM performed on the AgNP confirms the presence of individually charged AgNP and its expected variation (polarity and magnitude) with the Fermi level difference. Apart from establishing the selective charging of the AgNP, this thesis work also demonstrates the use of the charged, surfactant-free AgNP to perform charge-selective Raman scattering and fluorescence quenching for ionic analytes (fluorescein (-), rhodamine-6G (+) and acridine orange (+)). Furthermore, employing Atomic force microscopy (AFM) and optical absorption, it is established that the charging phenomenon plays an important role in self-inhibiting growth of Ag nanoparticles (AgNP) during chemical reduction. In particular, the positively charged AgNP do not coalesce despite a few nm interparticle spacing. Therefore, strong electromagnetic interactions between the particles develop, resulting in well resolved hybrid plasmon modes, probed by optical extinction. On the contrary, self-inhibition does not occur with negatively charged AgNP, resulting in the loss of surface plasmon resonance.

The thesis is organized as follows. Chapter 2 deals with a brief background on localized surface plasmon resonance and the formation of hybrid plasmons in nanostructures, discussing their role in chemical and biomedical sensing and signal enhancement, with particular impetus given to surface-enhanced Raman scattering. This Chapter also discusses the physics behind the charging mechanism of the AgNP. Chapter 3 describes, in detail, all the synthesis and characterization methods and conditions used to obtain the data in this thesis work. Chapter 4 presents the results of the study. In particular, AgNP charging and its role in self-inhibiting growth and coalescence of AgNP during electroless deposition, and charge-selective SERS are extensively described, as well as its impact on fluorescence quenching. Finally, in Chapter 5, in addition to drawing conclusions, future research possibilities and directions are briefly elucidated.

CHAPTER II

BACKGROUND

II.1) Localized Surface Plasmon Resonance and Hybrid Plasmons

Localized plasmons in metal nanoparticles can be described as the coherent motion of the conduction electrons under the influence of an oscillating electric field. Applying the principles of free electron theory of metals, a nanoparticle can essentially be treated as a bipartite system consisting of positively charged stationary atomic cores that are surrounded by free moving conduction electrons which possess an equal negative charge. When excited by an electromagnetic wave, the oscillating electric field causes the displacement of the conduction electrons which are subsequently restored to their equilibrium position due the Coulombic forces of attraction applied by the positively charged atomic cores. Therefore, these oscillations of the conduction electrons can be compared to a spring mass system whose resonance frequency $\omega_{\text{resonance}}$ is given by

$$\omega_{resonace} = \sqrt{\frac{k}{M}}$$

In the above equation, k is the effective force constant, and M is the mass of the electrons. However, if the frequency ω of the incident electric field is close, or equal to $\omega_{resonance}$, and the diameter of the nanoparticle $D << \lambda$,(wavelength of the incident field), the collective oscillations are maximized, leading to the formation of localized surface plasmon resonance(LSPR). This resonance results in strong coupling of incident radiation to the nanoparticle and electromagnetic field enhancements in its vicinity.

Electromagnetic field enhancements orders of magnitude higher than those observed in isolated nanoparticles are observed in monolayers of closely-spaced nanoparticles due to the formation of hybrid plasmons. For monolayers of nanoparticles with average diameter D, and interparticle spacing d, if $d/D << 1$, then under the influence of an electromagnetic field, the surface plasmons of individual NP can interact via two different configurations. The first is the anti-bonding configuration, caused by the negative parity of the dipole moments (anti-symmetric). Since the net dipole moment for the anti-bonding configuration is minimal (zero for identical particles), their light-coupling efficiency is drastically reduced, due to which they are referred as dark plasmons[23]. The second is the bonding configuration, caused by the positive parity of the dipole moments (symmetric electric fields). Since the net dipole moment for the above configuration is large, they couple efficiently with light, and are therefore referred as bright plasmons[23].

LSPR is sensitive to refractive index changes of the medium surrounding the NP, and this phenomenon is harnessed in sensing the presence of molecules, or variations in the concentrations of molecules around the NP, by measuring LSPR wavelength-shifts. In

addition, selectivity of LSPR sensors can be achieved by functionalizing the surface of the nanoparticle to detect the presence of only the molecules of specific interest.

For example, using nanosphere lithography (NSL)[24-26] to fabricate an array of triangular silver nanoparticles, Haes et al[4] have employed LSPR in the detection of Alzheimer's disease. It is believed that Alzheimer's disease is caused by self assembly of oligomeric assemblies of amyloid-β (Aβ) into soluble oligomers called amyloid-derived diffusible ligands (ADDL). The binding constant of ADDL with anti-ADDL antibodies was determined utilizing LSPR spectroscopy (i.e., measuring the frequency shift in plasmon modes). Further, by functionalizing gold nanoparticles with anti-EGFR (anti-epidermal growth factor receptor), and performing LSPR scattering and LSPR absorption, El-Sayed et al[27] have reported the ability to distinguish between cancerous cells responsible for oral cancer, and non-cancerous cells.

The phenomenon of LSPR results in intense field enhancement in the vicinity of silver and gold nanoparticles as their respective $\omega_{resonance}$ occurs in the visible region of the electromagnetic spectrum[28], enabling their use in Surface-enhanced Raman Scattering (SERS). Raman scattering by itself is an extremely inefficient process and its cross sections (10^{-30} cm^2) are 14 orders of magnitude smaller than those of fluorescent dyes (10^{-16} cm^2)[29]. However, effective Raman cross sections can be amplified by the field enhancement phenomenon displayed by noble metal nanostructures. The use of silver nanostructures in SERS was first reported by Fleischmann et al[30]. In their study, nanostructures obtained by chemically etching the surface of a silver electrode were responsible for the signal enhancement. This work was later corroborated in 1975[31], where the electric field enhancement mechanism for SERS was postulated. Xu et al[32]

have demonstrated that single molecule SERS sensitivity can be achieved by the adsorption of an analyte at the junction between two AgNP (dimer) that are separated by a distance of ≈ 1 nm. They estimate that using this configuration, enhancement factors of up to 2.5×10^{10} can be achieved that essentially renders the nanogap between the particles a "hot spot". Results from various other studies have strengthened the theory that significant increase of SERS enhancement can be obtained by adsorbing an analyte in between closely spaced silver and gold nanostructures[33-35].

One of the earliest and most commonly used methods for synthesizing monodisperse metal nanoparticles stabilized in the form of a colloidal suspension is the citrate reduction method[13, 36-38]. Although this method produces nanoparticles with controllable size and aggregation, the nanoparticles are coated with the stabilizing agent (heavy citrate ions and chlorine ions that are negatively charged electrical double layers). This surfactant can interfere with the analyte's signal as well as attenuate the electromagnetic enhancement or other surface-enhanced effects

Other methods that have been used to prepare arrays of metal nanoparticles for electromagnetic field enhancement include E-beam lithography[39], electrodeposition[40] and laser ablation[41, 42]. For the present thesis work, AgNP were synthesized using electroless deposition, which involves the formation of monolayers of AgNP by immersion of semiconductor films/wafers in a metal salt solution. The metal salt solution is reduced by the semiconductor substrate to produce surfactant-free and "clean", monodisperse nanoparticles[7, 18].

II.2) Metal on Semiconductor System

When a metal thin film is in contact with a semiconductor, at thermodynamic equilibrium, the individual Fermi levels of the metal and the semiconductor must be equal. Therefore, a charge transfer occurs between the metal and semiconductor. The magnitude and polarity of the charge transfer depend on the relative positions of the Fermi levels of the semiconductor (depends on doping, i.e., p-type or n-type) and the metal[43]. The energy band diagrams for a thin film of silver in contact with an n-type Si and p-type Si are shown below.

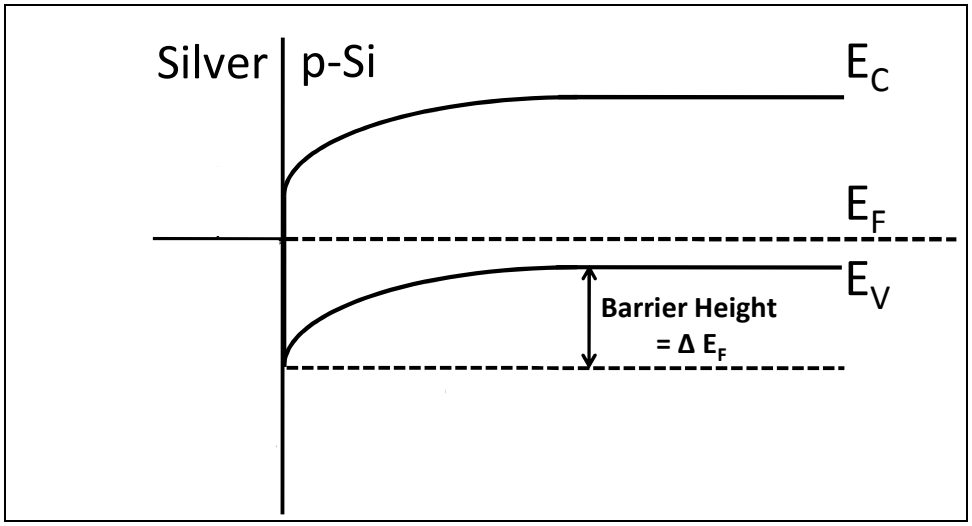

Figure 2.1. Energy band diagram for silver in contact with p-type Si.

In the case of p-type silicon, the addition of trivalent impurities (e.g., boron) trap valence electrons, creating empty valence states called holes, which cause the Fermi level E_F to be shifted to a lower level (Figure 2.1). Therefore, when silver, whose Fermi level is at a relatively higher level, is in contact with p-Si, silver loses electrons causing it to become positively charged.

However, the donation of free electrons to the conduction band by pentavalent impurities (e.g., phosphorous) in n-type Si causes its Fermi level to shift to a higher level (Figure 2. 2). Therefore, when silver is in contact with n-type Si, since the Fermi level of n-Si is at a higher level, the resulting electron transfer from n-Si to silver causes silver to get negatively charged.

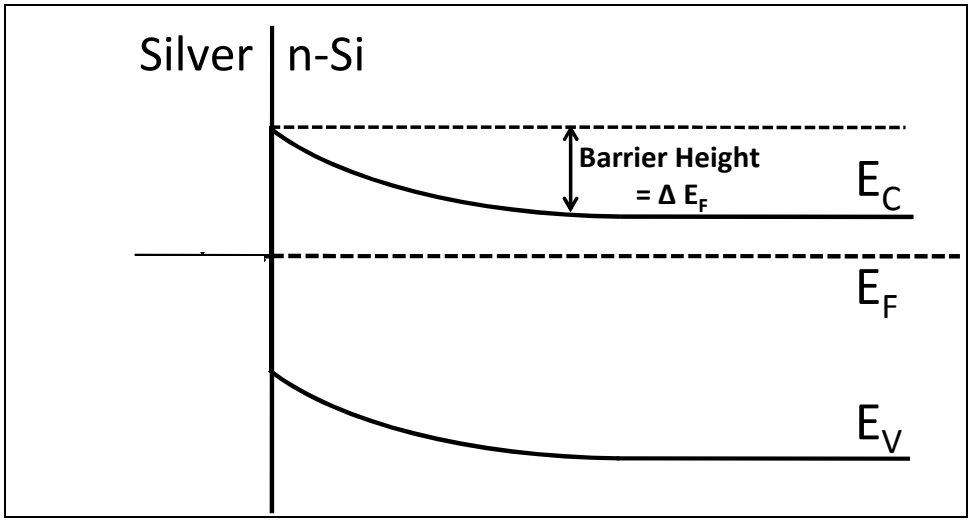

Figure 2.2. Energy band diagram for silver in contact with n-type Si.

The phenomenon of the selective charging of AgNP synthesized on p-type and n-type Si can be explained through the principles discussed above.

Further background information will be made available during discussion of the results if needed.

CHAPTER III

METHODOLOGY

III. 1) Overview

This chapter provides the processing and characterization details employed during the course of the present thesis work In this investigation, silver nanoparticles were synthesized on high conductivity p-type and n-type silicon wafers using two different techniques: 1). Electroless deposition, which involves the reduction of silver ions in a metal salt solution on silicon substrates, and 2) vapor deposition of silver on silicon wafers, followed by annealing. The synthesized nanoparticles were then characterized by atomic force microscopy (AFM), UV-Vis spectroscopy, Mie scattering, EFM, scanning electron microscopy (SEM), confocal laser scanning microscopy, and SERS, the details of which are disclosed below.

III. 2) Substrate Preparation

The substrate on which the nanoparticles were synthesized was p-type and n-type silicon wafers obtained from 'Silicon Quest International'. The p-type wafer had a diameter of 2", a <1-0-0> orientation and its resistivity was ≈ 0.001 - 0.005 Ωcm, while the n-type wafer had a 4" diameter, a <1-1-1> orientation and its resistivity was < 0.005 Ωcm.

The wafers were first rinsed with isopropyl alcohol (IPA) and de-ionized (DI) water, and then blow dried with nitrogen (N_2). The native oxide on the silicon wafers was removed by immersion in a 5% hydrofluoric acid (HF) solution for 10 minutes, followed by a de-ionized (DI) water rinse and N_2 blow dry.

III. 3) Nanoparticle Synthesis Using Electroless Deposition

Silver nanoparticles were synthesized as illustrated in Figure 3.1. The diced wafers (1 cm × 1 cm) were immersed in 0.002 M $AgNO_3$ + 0.1% HF solution for 60 s. The redox reaction was terminated by immersion of the wafers in DI water. AgNP are formed by a simple redox reaction involving the reduction of Ag^+ ions in the $AgNO_3$ by the silicon. HF is primarily used in the electroless deposition technique to continuously etch away the silicon oxide on the wafer that would otherwise form a barrier and impede silver's nucleation (i.e., redox reactions).

One limitation of EFM is its inability to resolve the potential profile of closely spaced (i.e., ≈ 50 nm or less) nanoparticles. To overcome this drawback, HF was not mixed in $AgNO_3$. Therefore, for characterization by EFM, the AgNP were reduced by

immersion of wafers in 0.02 M $AgNO_3$ solution for 10 s. In the absence of HF, nucleation was observed to be suppressed significantly. Similarly, gold nanoparticles (AuNP) conducive for EFM characterization were synthesized on n-type Si by immersion in 0.02 M $HAuCl_4$ for 10 s.

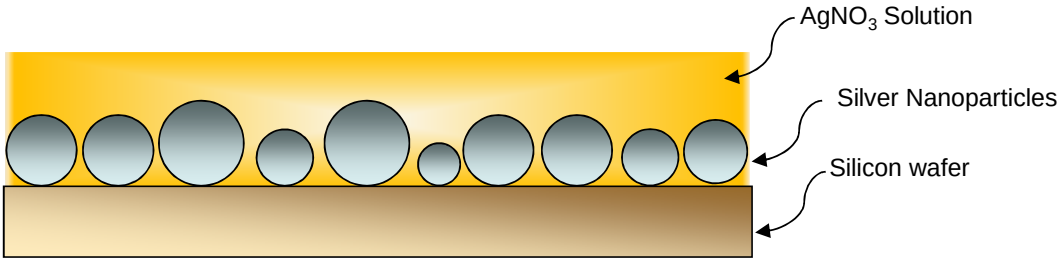

Figure 3.1. Sketch illustrating electroless reduction of silver nanoparticles on the silicon substrate.

III. 4) Nanoparticle Synthesis Using Vapor Deposition

For the physical vapor deposition (PVD) of silver, a Cressington 208C Vacuum Deposition System was utilized. The silver depositions were carried out at a base pressure of 4.5×10^{-5} mBar. Silver was thermally evaporated using a tungsten wire basket (wire diameter = 0.20 inches). The deposition rate was measured with a piezo-electric quartz crystal monitor. When the deposition rate was stabilized to 1 Å/s, the shutter covering the silicon wafers was opened, starting the deposition process. On depositing the required thickness of the silver film, 0.8 nm, the shutter was immediately closed, the electric current was gradually reduced, and the system was cooled down in vacuum, before being vented.

After the venting process, the wafers were blow dried with N_2 to remove any dust particles, and then placed on a hot plate maintained at 300°C for 5 min. The annealing

step was employed so that the thin irregular silver film deposited re-structures to monodisperse AgNP. The basic schematic of a vapor deposition system is illustrated below in Figure 3.2.

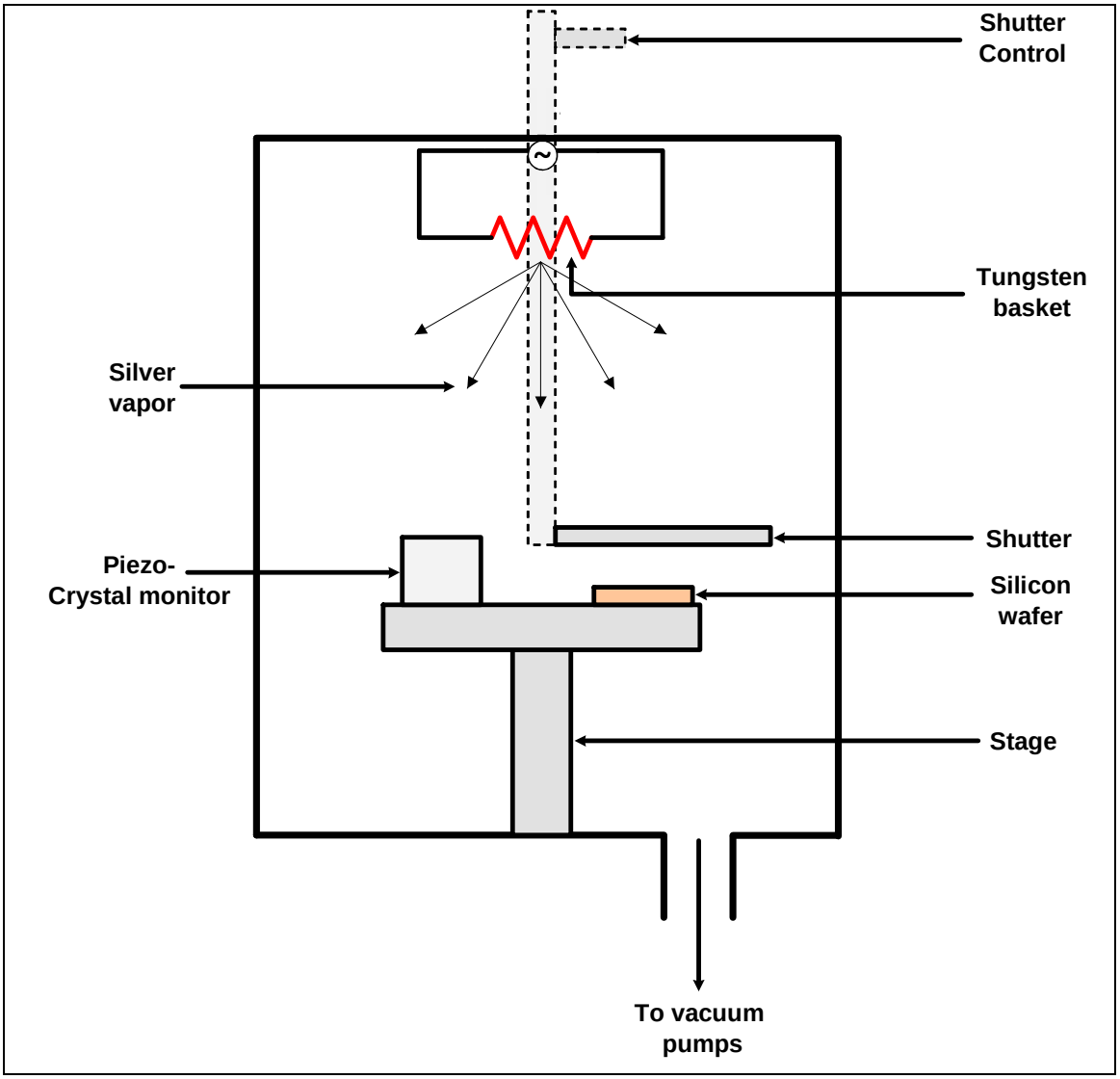

Figure 3.2. Illustration of the physical vapor deposition process.

III.5) Atomic Force Microscopy

The topography scans of the silver nanoparticles synthesized on the silicon wafers were performed using a Veeco Multimode V Scanning Probe Microscope, operated in the

TappingMode™ setting. The silicon wafers were stuck on a metal stub using a double sided sticky tape. The height measurements on the silicon substrates were obtained using a NSC 18 probe manufactured by 'MikroMasch'.

In obtaining clear AFM images, the cantilever and tip characteristics play a crucial role. For AFM, we used tips whose radius was 10 nm, with an aspect ratio greater than 3:1 and having a height of 15 µm. The scans were performed using a scan window area of 2 µm × 2 µm with a scan rate of 1 Hz. In order to obtain an image of good resolution, we used 256 sampling points per line.

III. 6) Electric Force Microscopy

EFM has established itself as a powerful non-destructive tool to characterize the electrostatic force characteristics of nanosized structures[44-49]. Over the years, EFM has successfully performed characterizations on a variety of electrostatic phenomena such as surface potential[50] and doping concentration in semiconductors[51]. In addition, EFM has been used in more specific cases, some of which include imaging the voltage characteristics of working microelectronic devices and in charge injection and detection of localized charge in nanostructures[52]. Furthermore, EFM has also extended to study the charge transport mechanisms in single NP embedded in insulating thin films[53-55].

EFM is essentially a modified atomic force microscope that, in addition to mapping height profiles of nanostructures, also can map out electrical properties of the nanostructure being studied. In a conventional AFM, the height profile is obtained either by a stationary or oscillating cantilever with a tip that is scanned over the nanostructure. In the case of the stationary cantilever, the force between the sample and tip is always

kept constant as the tip is scanned over the sample, and the presence of an object in the tips' path causes it to be lifted to a certain height which is proportional to establishing the constant force between the tip and sample. For the oscillating cantilever however, the presence of an object in the path of the scan changes the oscillating frequency of the cantilever. To restore the cantilever to its resonant frequency, the tip is lifted to a proportional height, which in the process characterizes the height of the object being scanned. In an EFM, after the height profile of the sample in a particular scan is acquired, a modified conductive tip, which is lifted to a certain height above the sample (100 nm), is scanned over the sample retracing the path generated during the AFM height scan. The lifted probe interacts with the sample through long-range Coulomb forces. This implies that any variations in the electrical characteristics (surface charge) in the sample are picked up by the oscillating cantilever with the conductive tip, which alters its oscillating frequency. The subsequent change made to restore the cantilever to its resonant frequency results in the electrical mapping of the sample.

Electric potential 100 nm above the surface of the synthesized nanoparticles (with respect to the high conductivity silicon wafer) was mapped using electric force microscopy (EFM). For EFM, a Veeco Multimode V Scanning Probe Microscope was used, fitted with a platinum coated NSC18 probe manufactured by MikroMasch. After aligning the tip, a window area of 2 µm × 2 µm was scanned, with a scan rate of 2 Hz, and a resolution of 512 data points per line.

III. 7) Scanning Electron Microscopy

The vapor deposited AgNP were imaged using a FEI Quanta 600 Scanning Electron Microscope. Since the samples being scanned were AgNP synthesized on high conductivity silicon wafers, charging effects were minimum that allowed a sufficiently high accelerating voltage (20 kV), with a working distance of 9.9 mm.

III. 8) Surface–enhanced Raman Spectroscopy

In order to explore the behavior of the charged AgNP on silicon wafers as SERS substrates, known concentrations of two ionic analytes, i.e., acridine orange (AO), a positively charged fluorophore, and fluorescein (F), a negatively charged fluorophore were used as analytes. Figure 3.3 shows the general schematic of Raman data collection mechanism. In particular, for our data acquisition, a WITec alpha300 M Raman system was used.

1 µL aliquots of AO (1.3×10^{-6} M) and F (1×10^{-7} M) were spotted on the vacuum deposited AgNP on the p-type and n-type silicon wafers. Using a 20× lens the laser was manually focused at the aliquot/substrate interface. The analyte was excited by an Ar^{+} ion laser, at a wavelength of 532 nm, whose incident excitation power was measured at 2.6 mW. The signal was integrated for 50 s.

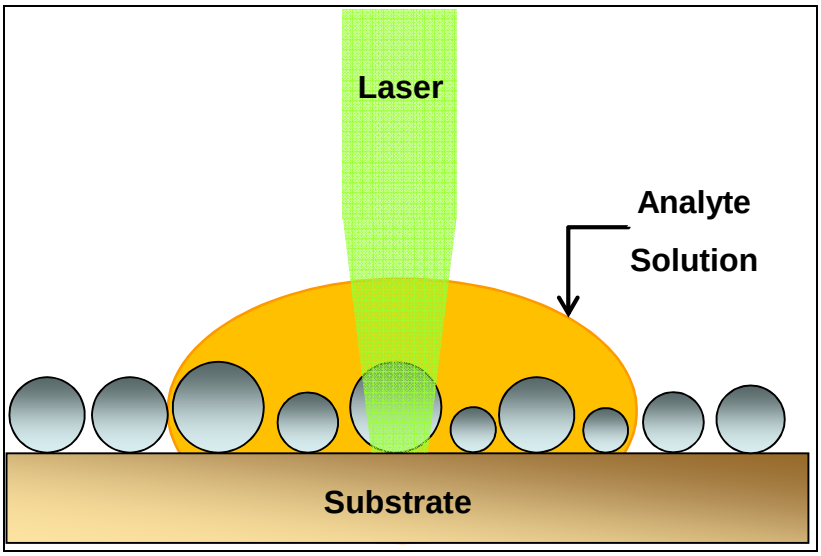

Figure 3.3. Demonstration of laser exposure of analyte and SERS data collection. (Courtesy: Dr. Kaan Kalkan).

III.9) Confocal Laser Scanning Microscopy

Further investigation of the charging of the AgNP was conducted by photoluminescence measurements. Confocal laser scanning microscopy scans of F and rhodamine-6G (R6G), a positively charged fluorophore, spotted on AgNP deposited on the p-type and n-type silicon wafers were performed, using a Leica TCS SP2 Confocal Microscope System. This system was fitted with a Leica DM E14 upright microscope with a 10× objective lens. 1 µl aliquots of F (1×10^{-7} M) and R6G (1×10^{-8} M) was spotted on the AgNP deposited on the respective silicon wafers. R6G was excited using a 514 nm Ar^{+} laser, and F was excited using a 488 nm Ar^{+} laser for resonant excitation of the fluorophores. The time series scans were taken at 1 s intervals.

III.10) UV-Vis Spectroscopy

Time series optical extinction of AgNP was acquired in real time during electroless reduction using a StellarNet EPP 2000Cs UV-Vis spectrophotometer fitted with a CCD detector. For this investigation, amorphous silicon films deposited on transparent glass substrates were used as the reducing agent. The semitransparent films enabled the UV-Vis optical transmission measurements from which extinction was derived. Extinction can be expressed as,

Extinction = - log (Transmission)

The amorphous Si films were prepared by chemical vapor deposition (Penn State MCL). H_2 diluted silane (H_2:SiH_4) (20.8:1) was employed as the precursor. The deposition was carried out at a substrate temperature of 120 ºC and a power of 120 Watts. The pressure was maintained at 5 Torr and the deposition time was 60 s.

The amorphous silicon thin film has a relatively lower Fermi level, similar to p-type Si. After dicing the Si film to the required size (0.5 cm × 2 cm), it was inserted into the PMMA optical cell and fixed in place using a steel spring. In order to obtain the optical extinction measurements of the AgNP, the extinction of silicon substrate without nanoparticles was subtracted from the extinction of silicon substrate with nanoparticles. The subtraction was carried out by the Spectrawiz software that is bundled with the optical spectrometer. The in-situ monitoring of the AgNP synthesis kinetics was initiated by introducing 0.002 M $AgNO_3$ + 0.1% HF into the PMMA optical cell containing the Si film, and episodically capturing the optical extinction spectra of the synthesized AgNP in 2 s intervals (computer time). In order to maximize the signal to noise ratio, the detector

integration time was set at 75 ms, and 2 scans were averaged per episode. The total duration of the episodic capture was measured to be 136 real seconds (120 intervals).

III.11) Mie-Scattering Measurements

Mie scattering of the AgNP synthesized on p-type and n-type silicon was measured using a Renishaw RM 1000 Raman system. The AgNP were synthesized using electroless reduction as mentioned in Section III.3. Tungsten halogen illumination was focused on the AgNP using a 20× lens, which also collected the scattered radiation in the backscattering geometry. The scattered intensity is computed using quartz as the reference. Backscattering from quartz is essentially specular reflectance, which is close to constant at ~ 6 % in the entire visible range. To perform backscattered measurements, a 150 lines/mm grating was used, and the integration time was set at 100 s. Although the integration times were set at the same in these measurements, the illumination intensity and collection efficiency was varied, so that saturation of detector did not occur.

CHAPTER IV

RESULTS & DISCUSSIONS

IV.1.) EFM Characterization and Nanoparticle Charging

Figure 4.1 (a) shows a representative 3D AFM height map of silver nanoparticles synthesized on p-type Si. Here, due to inability of EFM to resolve closely spaced nanostructures less than 50 nm, AgNP with sufficient interparticle separation were synthesized by immersion of Si in pure $AgNO_3$ solution for 10 s, as described in Chapter 3. During a typical electroless reduction process, HF is mixed in the $AgNO_3$ solution to continuously etch the oxide that forms on the surface of the silicon. This silicon oxide layer is the product of the oxidation reaction and it prevents further nucleation once a conformal layer forms. Therefore, the lack of HF in the $AgNO_3$ solution leads to limited nucleation and formation of well-separated (average particle separation distance ≈ 500 nm) but larger (average particle size ≈ 120 nm) AgNP, which could be successfully resolved by EFM.

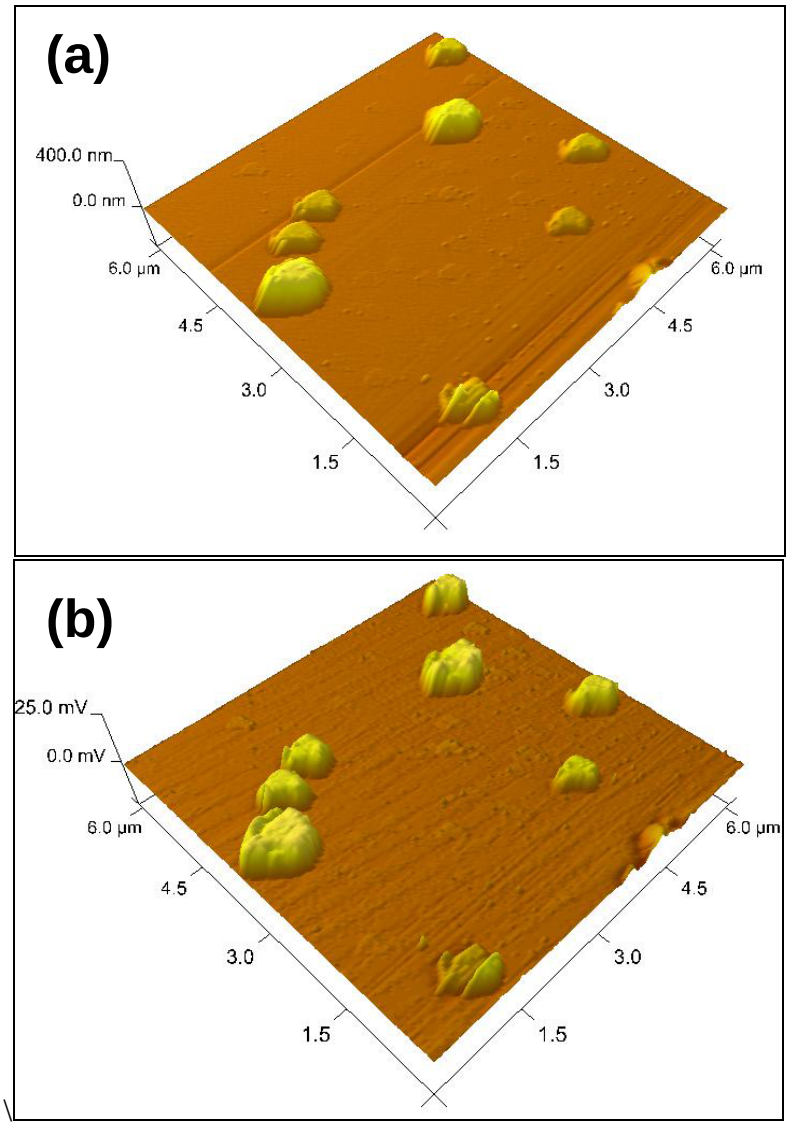

Figure 4.1. (a) 3D view of an AFM height map of AgNP deposited on p-type Si (operated in TappingMode™) **(b)** Corresponding 3D view of the EFM potential map.

In Figure 4.1 (b), the corresponding electric potential map of AgNP is shown at 100 nm above the surface. Here, the protrusions clearly indicate that the AgNP synthesized on p-type Si are positively charged. This positive charge is induced by Fermi level difference between silver and p-type Si. For AgNP synthesized on for p- type silicon, the Fermi level of silver is at a higher energy than that of p-Si, causing AgNP to donate electrons to Si, thereby acquiring a positive charge. The work function of silver is

4.3 eV. For heavily-doped p-Si, Fermi level is expected to be at about the valence band edge, which is 5.15 eV below vacuum level resulting in a Fermi level difference of (ΔE_F) $\approx$ 0.85 eV[43, 56, 57].

To further elucidate the impact of Fermi level difference on nanoparticle charging, AgNP were synthesized on n-type Si incorporating the same synthesis parameters used for synthesizing AgNP on p-type Si. Similarly, Figure 4.2 (a) shows a representative 3D height map of AgNP synthesized on n-type Si. As observed, immersing n-type Si in 0.02 M $AgNO_3$ for 10 s yields well-spaced AgNP (average size $\approx$ 14 nm, and average interparticle separation distance $\approx$ 200 nm), suitable for EFM characterization.

Figure 4.2 (b) depicts the corresponding electric potential map where the EFM scan was again conducted 100 nm above the surface. This time, depressions are observed which are indicative of negatively charged AgNP. Similar to the case of positively charged AgNP, the negative charge acquired by AgNP is also attributed to the Fermi level difference. However, the Fermi level of silver is lower than the Fermi level of heavily doped n-Si. Consequently, thermodynamic equilibrium is established by electron transfer from latter to former causing AgNP to acquire a negative charge. For heavily-doped n-Si, the Fermi level is expected to be at about the conduction band edge, which is 4.05 eV below the vacuum level Hence, the Fermi level difference between silver and n-Si, (ΔE_F) is about - 0.25 eV.

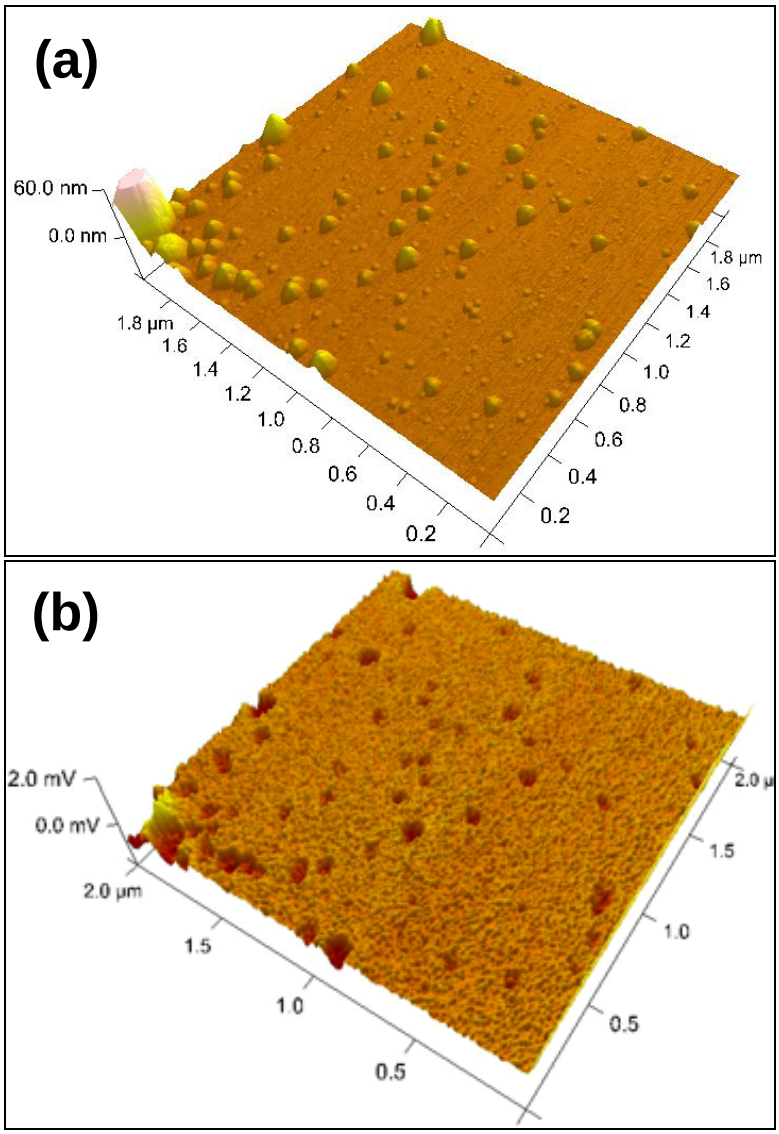

Figure 4.2. **(a)** 3D view of an AFM height map of AgNP deposited on n-type Si (operated in TappingMode™), **(b)** Corresponding 3D view of the EFM potential map.

In order to establish that the Fermi level difference induced selective charging can also be extended to other metal NP on semiconductor systems, EFM was performed on gold nanoparticles (AuNP), which were synthesized on n-type Si employing electroless reduction.

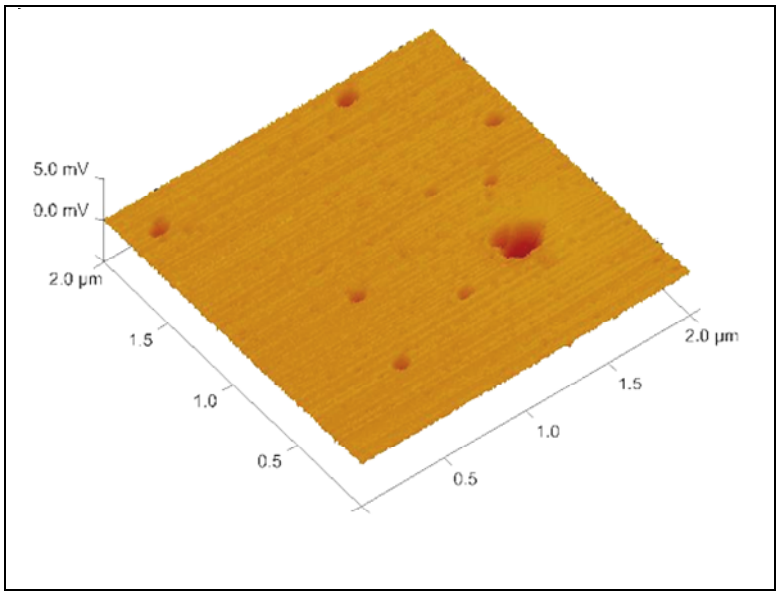

Figure 4.3. 3D view of an EFM potential map for AuNP synthesized on n-type Si.

Depressions in the electric potential map of AuNP synthesized on n-Si (Figure 4.3) confirm the presence of negatively charged AuNP. Owing to Fermi level difference between gold[58] ($E_F \approx 5.3$ eV below vacuum level) and n-Si ($E_F \approx 4.05$ eV below vacuum level), electrons flow from n-Si (higher Fermi level), to the gold nanoparticles (lower Fermi level) upon contact. This causes the AuNP to acquire a negative charge ($\Delta E_F \approx -1.25$ eV).

Furthermore, in either positively or negatively charged metal NP, the underlying substrate (Si) region is oppositely charged. The resulting Coulombic attraction is anticipated to anchor the nanoparticles to the Si substrate.

IV.2) Nanoparticle Size v/s Potential

Size v/s potential analysis performed for individual AgNP on Si revealed a monotonous relationship. The analysis was carried out using the Nanoscope 7.20 software integrated with the Veeco AFM. The results for positively and negatively charged AgNP are displayed in Figures 4.4 a and b, respectively. Here, the AgNP electric potential is measured at 100 nm away from the surface and corresponds to the center of the particle's projection on the xy plane.

It is observed that the magnitude of AgNP potential (100 nm away from the surface) increases with increasing size. To better understand the relationship, a simple model was constructed. Assuming that for a charged nanoparticle, the majority of the charge accumulates at the interface with silicon, the opposite charge layer couple at the Ag/Si interface behaves as a dipole.

For p-Si, having a resistivity of 0.005 Ωcm, the value of the doping density N_D is calculated to be ~ 3×10^{18} cm^{-3}using the relation

$$N_D = (q\mu_P\rho)^{-1} \tag{4.1}$$

where,

q = electron charge (1.6×10^{-19} C)

μ_P = Hole Mobility (440 cm^2 V^{-1} s^{-1})

For the calculated value of N_D , the depletion width W is calculated to be ~ 20 nm using the equation[43]

$$W = \sqrt{\frac{2\varepsilon_s}{qN_D}(V_{bi} - V - \frac{kT}{q})} \tag{4.2}$$

Where,

ε_s is the permittivity of the semiconductor substrate

$V = \Delta E_F$, which is the Fermi level difference

However, EFM measures the potential of the NP at a height 100 nm above the surface of the NP having a height of *R*. Then, for a dipole, and at a point *L* = 100 nm above the NP surface, the potential is given by

$$\Phi_{EFM} \approx \frac{Q(W/2)}{4\pi\varepsilon_o(R+L)^2} \tag{4.3}$$

where, *W/2* is the dipole separation distance, while the center of the dipole is approximated to be at the interface.

For a NP of hemispherical shape having a height (radius) equal to *R*, *Q* can be calculated as

$$Q = eN_dW(\pi R^2) \tag{4.4}$$

From equations 4.3 and 4.4, the potential of a nanoparticle synthesized on a doped semiconductor substrate, at a point 100 nm away from the surface of the nanoparticle can be expressed as

$$\Phi_L = A\frac{R^2}{(R+L)^2} \tag{4.5}$$

Where, *A* is the appropriate constant.

Using the above equation, and from the values obtained using EFM, *A* is obtained by the minimization of the square error. The calculated values for *A* for AgNP

synthesized on p-type Si (A_P) and n-type Si (A_N) was 36.51 and 18.52 respectively. The fits are represented by the red lines on the respective plots. In the case of negatively charged AgNP (Figure 4.4(a)), the potential of the AgNP is low enough to be significantly affected by initial calibration error in the EFM in terms of a constant baseline. Accordingly, a baseline of 3.5×10^{-4} V is subtracted from the measured values of AgNP potential for the best fit.

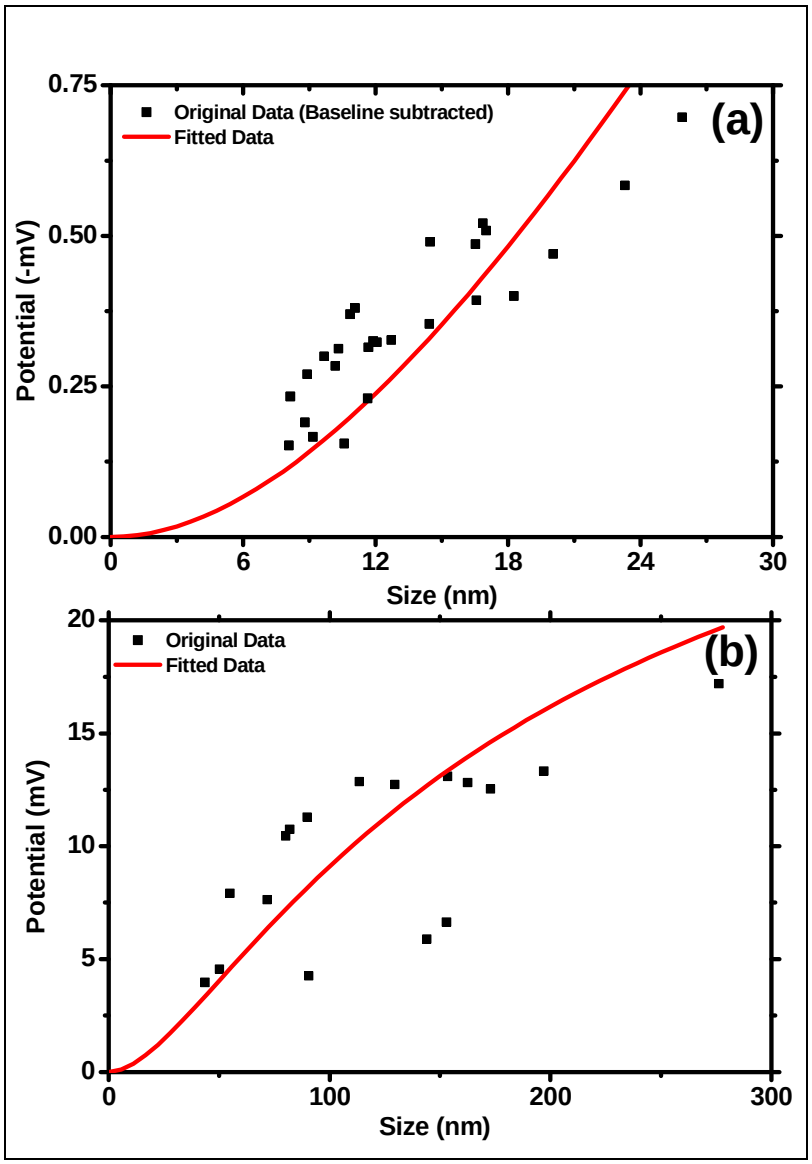

Figure 4.4. Graph illustrating the relation between nanoparticle size and potential with the calculated fit for AgNP synthesized on **(a)** n-type Si (baseline subtracted), and **(b)** p-type Si.

The data in Figure 4.4(b) show that the potential of the AgNP tends to saturate with the increasing size of the NP. For negatively charged AgNP however (Figure 4.4(a)), the size of the AgNP and their corresponding potential is an order of magnitude less than those observed for positively charged AgNP. Owing to this disparity, the fit obtained for negatively charged AgNP is in the linear regime of the fit obtained for positively charged AgNP, and thus does not show saturation.

The above described mathematical model tries to provide a basic understanding of the relation between NP size and its potential. As the data obtained from EFM is the potential of the AgNP at a distance of L=100 nm above the surface of the AgNP, the mathematical analysis was performed accordingly. However, in equation 4.5, if L=0, (i.e., at the surface of the AgNP), the theoretical value of the potential remains constant for all sizes of AgNP.

This discrepancy sources from the simplicity of the dipole model, which neglects the 3D geometry and assumes all metal charge is located at the interface. On the other hand, in a metal all internal fields must be essentially zero at equilibrium. Hence, by Gauss law, the charge density inside the metal is also zero. Accordingly, a surface charge distribution on the metal is necessary to counterbalance the field created by the interface dipole. Effectively, this surface charge increases the dipole separation. Therefore, the dipole separation does not equal *W/2* and it is a function of size of the nanoparticle, R. Therefore, equation 4.5 can be corrected as,

$$\Phi_L \approx \frac{AR^2(d_0 + f(R))}{(R+L)^2} \tag{4.6}$$

where,

d_0 is a constant, and $f(R)$ is the correction for dipole separation which varies with the NP size (R).

Therefore, at the surface of the NP, $L = 0$, and equation 4.6 reduces to

$$\Phi_S = A(d_0 + f(R)) \tag{4.7}$$

Equation 4.7 gives the approximate theoretical variation of the surface potential of the AgNP, with the corresponding variation in NP size.

IV.3) Impact of NP charging: Self-Inhibition of AgNP Coalescence (Electroless deposition)

The episodic monitoring of the electroless reduction of AgNP on a hydrogenated amorphous silicon film (a-Si:H) is shown in Figure 4.5 in terms of optical extinction. Each episode is captured at intervals of 2 s, beginning from the time of the introduction of the metal salt solution (0.002 M $AgNO_3$, + 0.1% HF) into the optical PMMA cell enclosing the a-Si:H film on glass substrate. The spectra were captured for a total time period of 136 s. As the reaction proceeds, the height of the regular plasmon and the hybrid plasmon peaks gradually increase, indicating the strengthening of LSPR.

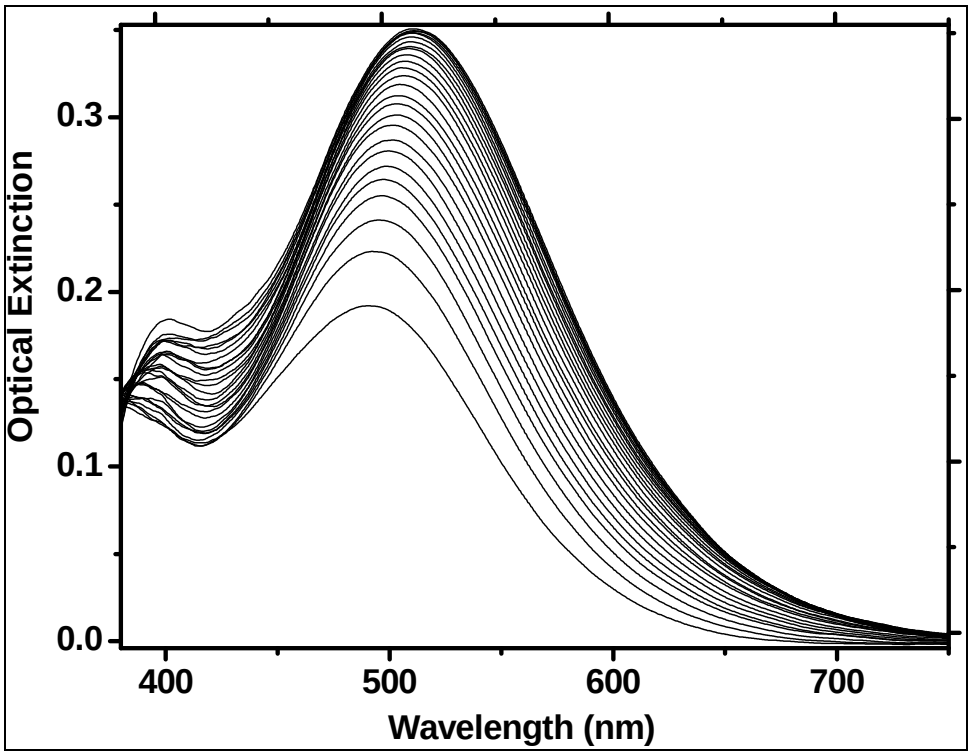

Figure 4.5. Episodic capture of the optical extinction spectra of AgNP synthesis on high band gap amorphous Si.

Also evident in Figure 4.5, is the relative shifts of the peak positions of both, regular and hybrid plasmon peaks. The normal plasmon peak shifts from an initial position of 386 nm to a position of 402 nm at saturation, a total red shift of 16 nm. Similarly, the hybrid plasmon peak shifts from an initial position of 490 nm to 512 nm at saturation, a shift of 22 nm. These shifts are represented in the waterfall plot of the episodic capture, which is shown in Figure 4.6.

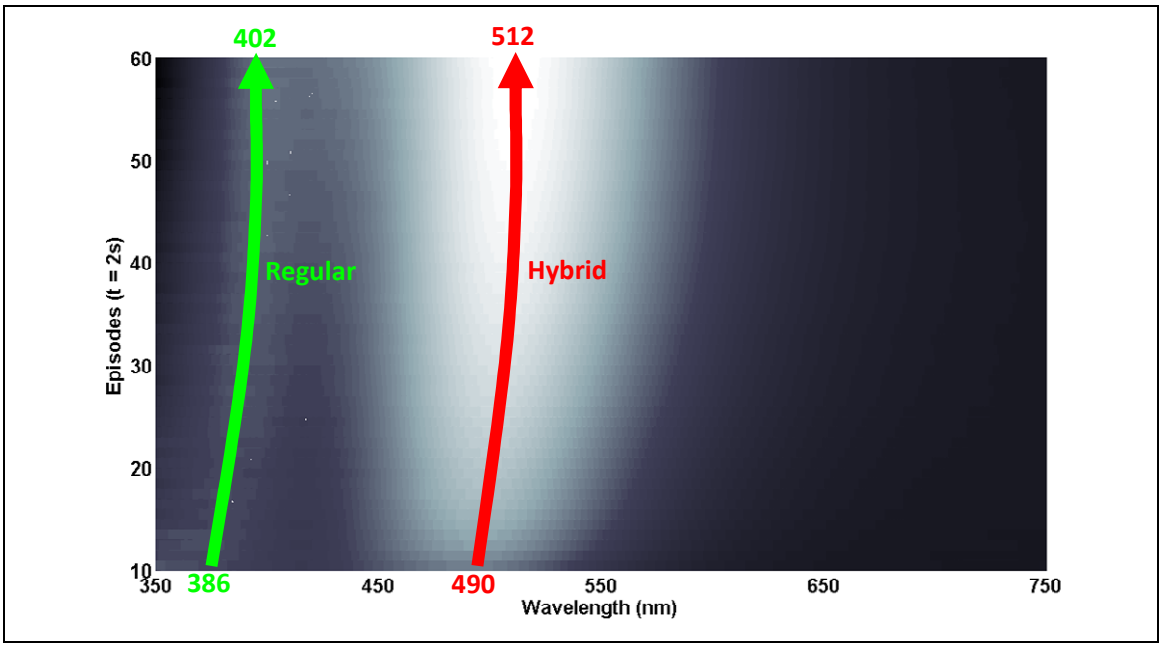

Figure 4.6. 3D waterfall plot of the episodic capture of synthesis of AgNP on high band gap amorphous Si. The relative shifts of the regular and hybrid plasmon peaks are also represented.

The red-shift of the regular plasmon peak indicates an increase in average AgNP size during growth, as expected. Furthermore, the red-shift of the hybrid plasmon peak indicates an increase in interparticle electromagnetic interaction (i.e., hybridization), which is attributable to increased size as well as reduced interparticle separation. The presence of the hybrid plasmon peak even at saturation confirms that: although the particles grow, they never coalesce, thereby sustaining the LSPR. This phenomenon can be attributed to the charging of the individual AgNP. Compared to silver, the Fermi level of the intrinsic a-Si:H film is at a lower energy: a case similar to that with p-type silicon. Typically, a-Si:H has a higher bandgap of ~1.8 eV. Hence, the Fermi level for the intrinsic material should be at the midgap. Namely, it is estimated to be ~ 4.9 eV below the vacuum level. Therefore, the AgNP lose electrons to Si, and are expected to acquire a

positive charge (Section IV.1). This positive charging of the AgNP leads to self - inhibiting growth of AgNP synthesized using electroless deposition.

The self inhibition due to NP charging can be explained using a Pourbaix diagram of the reduction reaction, shown in Figure 4.7. The x-axis represents the pH of the reaction, for which the reduction reaction has no dependence. The y-axis represents the voltage externally applied on the reaction. As mentioned in Section III.3, AgNP are formed by the reduction of Ag^+ by silicon (i.e., $Ag^+ + e^- \rightarrow Ag$). The solid horizontal line in the Pourbaix diagram represents this reduction reaction in equilibrium with the external voltage at which the net reduction (AgNP synthesis) is stopped. The reduction occurs below the line, and is reversed to oxidation above the line.

In the case of positively charged AgNP, nanoparticle growth causes an increase in NP potential. On sufficient growth of the AgNP, like charges between the AgNP and the deposition ions Ag^+ cause the repulsion of silver ions. This reduction in $[Ag^+]$ lowers the reduction potential of the reaction given by the Nernst Equation as given below.

$$\Phi_{Ag} = \Phi^{o}_{Ag} + \frac{RT}{F}\ln[Ag] \tag{4.7}$$

Therefore the reduction potential of the reaction is reduced, or the solid line of the Pourbaix diagram shifts down. Furthermore, as the particles grow bigger, due to the increasing potential of the AgNP, the nanoparticle voltage applied on the reaction (V) increases, as represented by the dashed line in Figure 4.7. Once the nanoparticle voltage (V) overlaps with the reduction potential, the opposing voltages (nanoparticle voltage and

the reaction voltage) balance each other out, resulting in the self-inhibition of the reaction.

For negatively charged AgNP however, the opposite charges between the AgNP (-) and deposition ions Ag^+, cause the reaction to proceed without any impediment (i.e., the reduction potential increases). Additionally, the negative charge on the AgNP lowers the nanoparticle voltage applied on the reaction. Hence, the two opposing forces never coincide and counterbalance each other. Namely, the solid line and the dashed line in the Pourbaix diagram diverge. As a result, the reduction reaction proceeds until the individual AgNP coalesce.

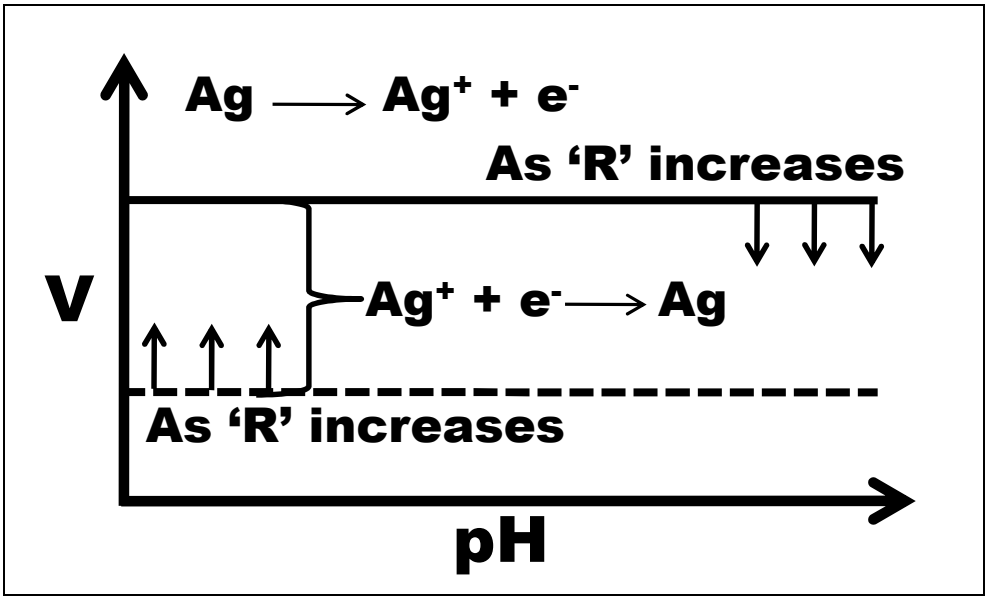

Figure 4.7. Schematic of effect of nanoparticle charging on the reduction reaction.

The effect of self-inhibition of the reduction reaction was established by performing AFM on AgNP synthesized on p-type and n-type Si. AgNP were synthesized on the respective silicon substrates by immersion in 0.002 M $AgNO_3$, + 0.1% HF for 60 s.

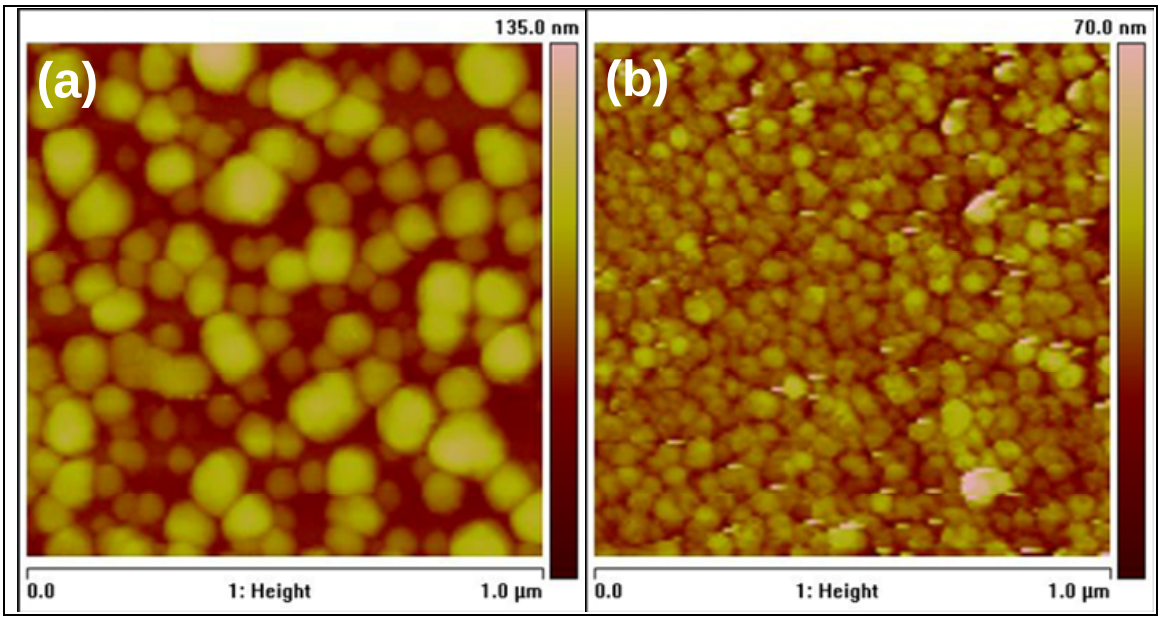

Figure 4.8. AFM height maps of silver nanoparticles synthesized on **(a)** p-type silicon and **(b)** n-type silicon. The scans confirm the difference in the morphology and density of the synthesized AgNP on both the wafers, despite keeping the exact synthesis parameters.

Figure 4.8 (a) shows an AFM height scan of AgNP synthesized on p-type Si. As explained above, since the AgNP are positively charged, the reaction is self inhibited with the presence of relatively large AgNP (~ 40 nm) that do not coalesce. However, for AgNP synthesized on n-type Si, (Figure 4.8(b)) smaller AgNP (~10 nm) are observed that display no interparticle separation, confirming the role of AgNP charging on the self inhibiting coalescence of AgNP synthesized using electroless deposition.

As evidenced from Figure 4.8(a, b), employing electroless reduction results in a distinct difference in the size and morphology of AgNP synthesized on p-type and n-type Si. Due to self-inhibition of AgNP coalescence, positively charged AgNP display interparticle separation (few nm), which should result in LSPR. In contrast, negatively charged AgNP coalesce with each other. As a result, LSPR is expected to be lost. This

postulated difference in LSPR between AgNP synthesized on p-type and n-type Si was confirmed by Mie-scattering.

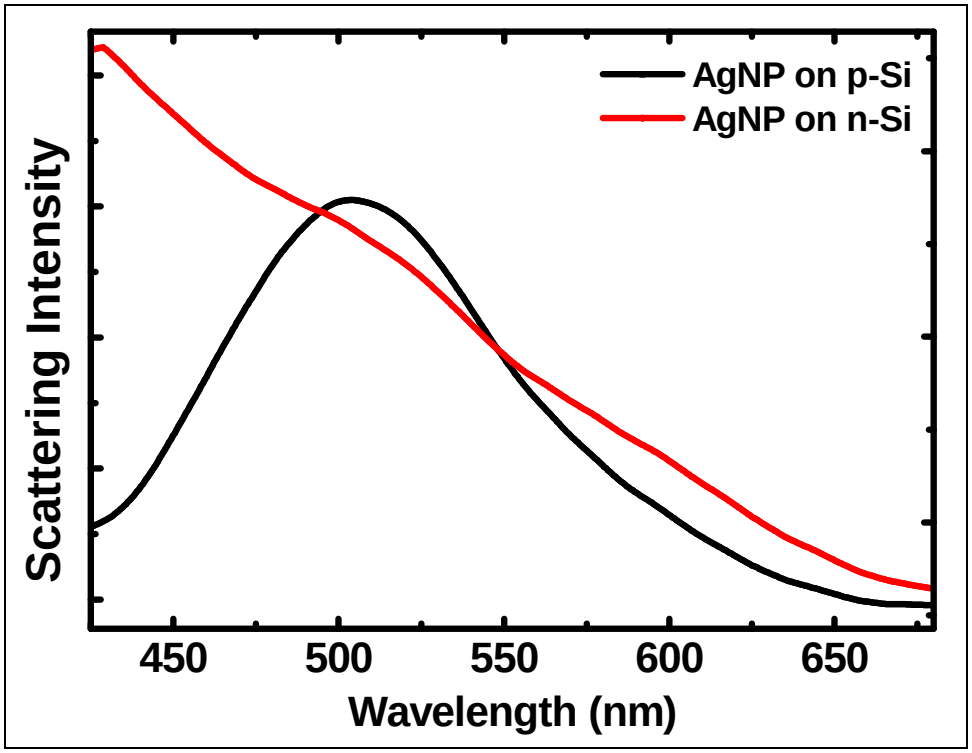

Figure 4.9. Back-scattered measurements showing SPR of AgNP deposited on p-type Si (black) and n-type Si (red).

Figure 4.9 clearly confirms the expected difference in LSPR of positively and negatively charged AgNP synthesized using electroless reduction. For AgNP synthesized on p-Si, a clear, well resolved plasmon peak is observed at ~ 510 nm. However, for negatively charged AgNP, due to nanoparticle coalescence, the LSPR does not develop.

These measurement results lead to the conclusion that owing to the selective charging of the AgNP, while employing electroless reduction, only positively charged metal NP reduced on a semiconductor (i.e., Fermi level of the metal is higher than the

Fermi level of the semiconductor) display LSPR, and can be used as SPR sensors / SERS substrates.

IV.4) Impact of NP Charging: Charge-selective Raman Scattering

Another important motivation of this work has been to harness this selective charging of the nanoparticles in fabricating charge-selective SERS substrates. Since SERS is affected by the morphology of the substrates, the difference in morphologies of the AgNP synthesized by electroless reduction makes the comparison of positively charged and negatively charged AgNP as charge-selective SERS substrates difficult.

To overcome the issue of dissimilar morphologies of AgNP synthesized on p-type and n-type Si, and to further explicate the effect of nanoparticle charging in SERS, AgNP were synthesized on Si using vapor deposition. The morphology of the vapor deposited AgNP was imaged using a FEI Quanta 600 Scanning Electron Microscope.

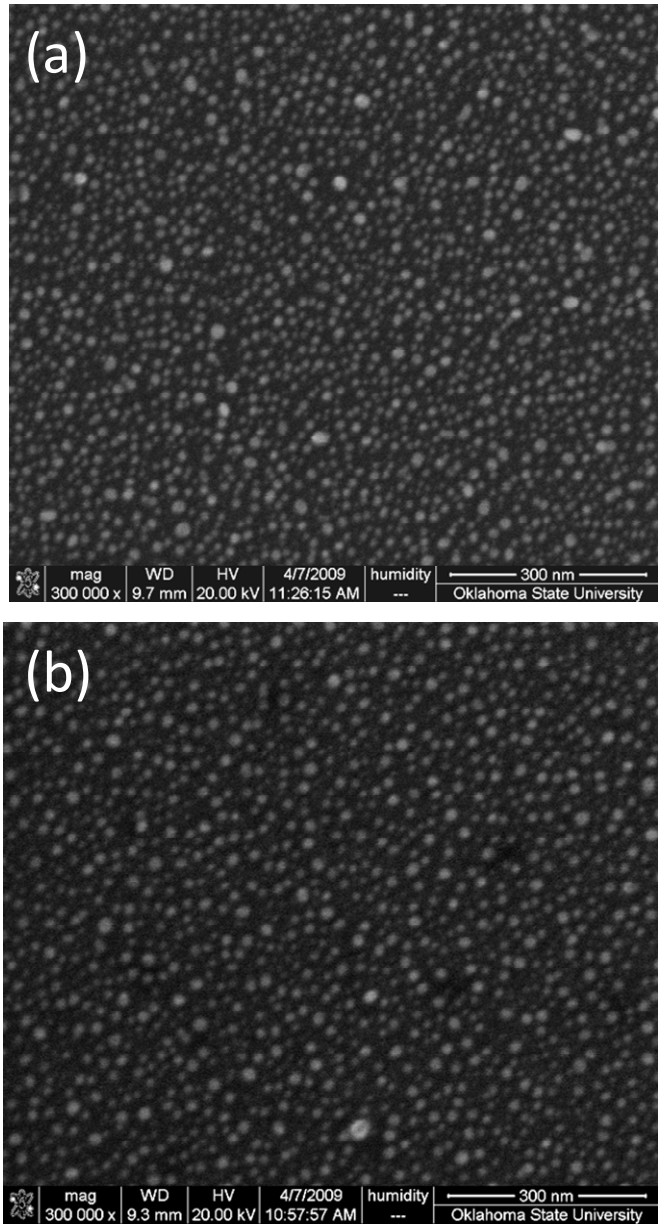

Figure 4.10. SEM micrograph of vapor deposited AgNP on **(a)** n-type Si, and **(b)** p type Si.

The SEM scan of vapor deposited AgNP on n-type Si, as shown in Figure 4.10 (a), confirms the presence of monodisperse AgNP, with an average particle size of ~ 20 nm. AgNP vapor deposited on p-type Si display a similar morphology to those synthesized on n-type Si, having an average particle size of ~ 20 nm (Figure 4.10 (b)). The similar morphologies, coupled with selective charging of the AgNP enables the

comparison of the vapor deposited AgNP on the p-type and n-type Si as charge-selective SERS substrates.

Figure 4.11 shows a SERS spectra acquired from 1×10^{-7} M fluorescein[7] (F) spotted on p-type silicon (black curve), and 1×10^{-7} M F spotted on n-type silicon (red curve). F is a negatively charged fluorophore, with an absorption maximum at 494 nm and emission maximum of 521 nm. It is hypothesized that owing to Coulombic interaction between the analyte and charged substrates, negatively charged fluorescein molecules would be strongly adsorbed on the surface of the positively charged AgNP, than negatively charged AgNP.

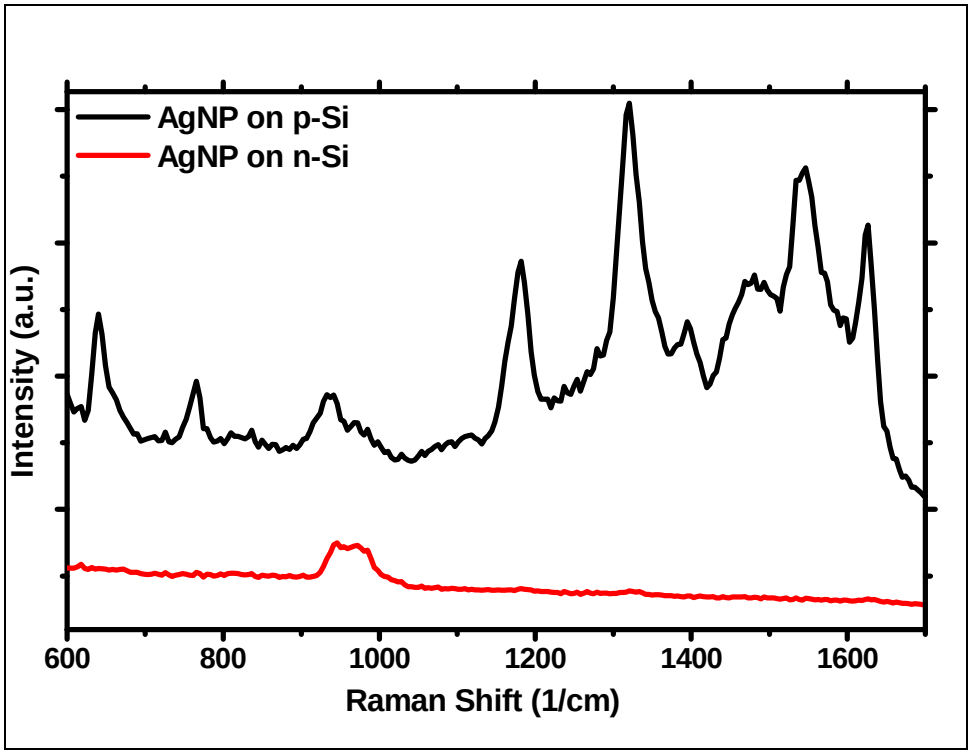

Figure 4.11. SERS spectra of 1 µl of fluorescein (1×10^{-7} M) spotted on p-type silicon (black) and n-type silicon (red).

SERS spectra observed in Figure 4.11 confirm this prediction of positively charged AgNP being selective SERS substrates for F. In both cases, the acquisition parameters were kept the same (Section III.8). Obviously, for F spotted on positively charged AgNP, distinct Raman peaks for fluorescein are observed, as compared to absence of peaks for F spotted on AgNP deposited on n-type silicon. This is due to the presence of NP charge, that either strongly attracts, or repels the analyte molecules. In this particular case, positively charged AgNP attract the negatively charged F ions to its surface due to Coulombic forces of attraction, which results in the signal enhancement. In contrast, negatively charged AgNP repel the F molecules, keeping them away from the vicinity of the nanoparticle that is associated with high SERS gains, resulting in the disappearance of Raman peaks. It should be noted here, that the broad peak at ~ 950 cm^{-1} observed in the red spectrum is the second order Raman scattering peak of silicon[59], and is not indicative of the Raman scattering signal of the analyte (fluorescein). Figures 4.12 and 4.13 illustrate the schematic of fluorescein molecules getting attracted to or repelled away in the case of positively and negatively charged AgNP.

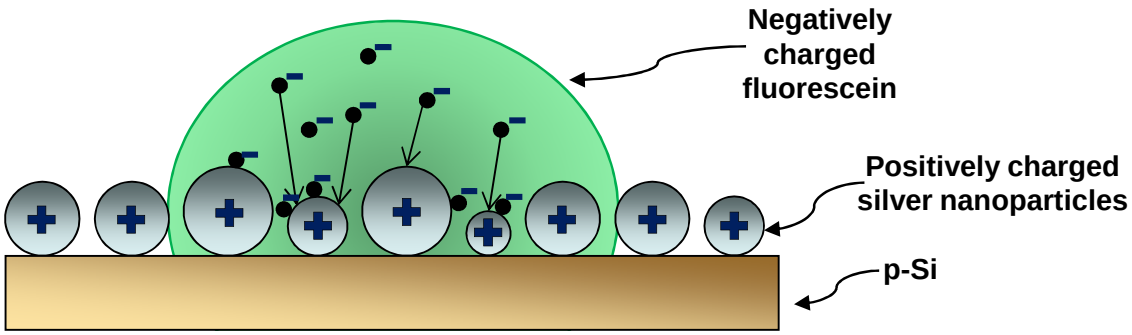

Figure 4.12. Schematic of fluorescein molecules getting attracted to positively charged AgNP.

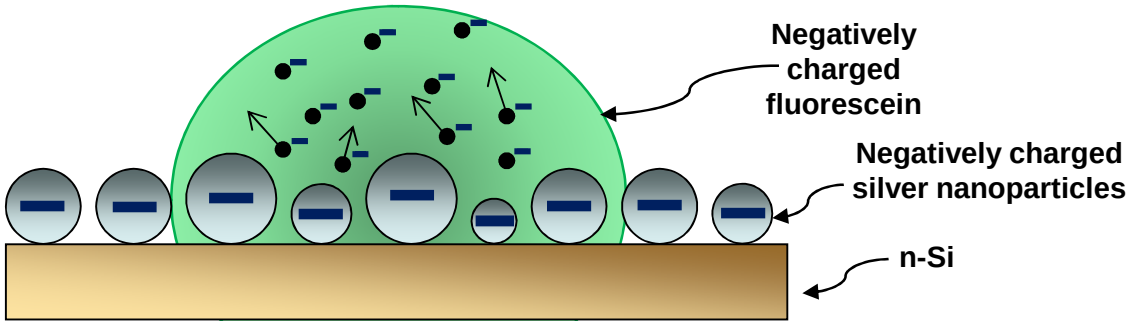

Figure 4.13. Schematic of fluorescein molecules getting repelled away from negatively charged AgNP.

To further establish the impact of nanoparticle charging on SERS, acridine orange (AO)[60], a positively charged fluorophore, was spotted on positively and negatively charged AgNP, and SERS was performed. AO was chosen as an analyte for SERS as its absorption maximum at 488 nm and emission maximum at 526 nm is similar to that of fluorescein, but is opposite in charge.

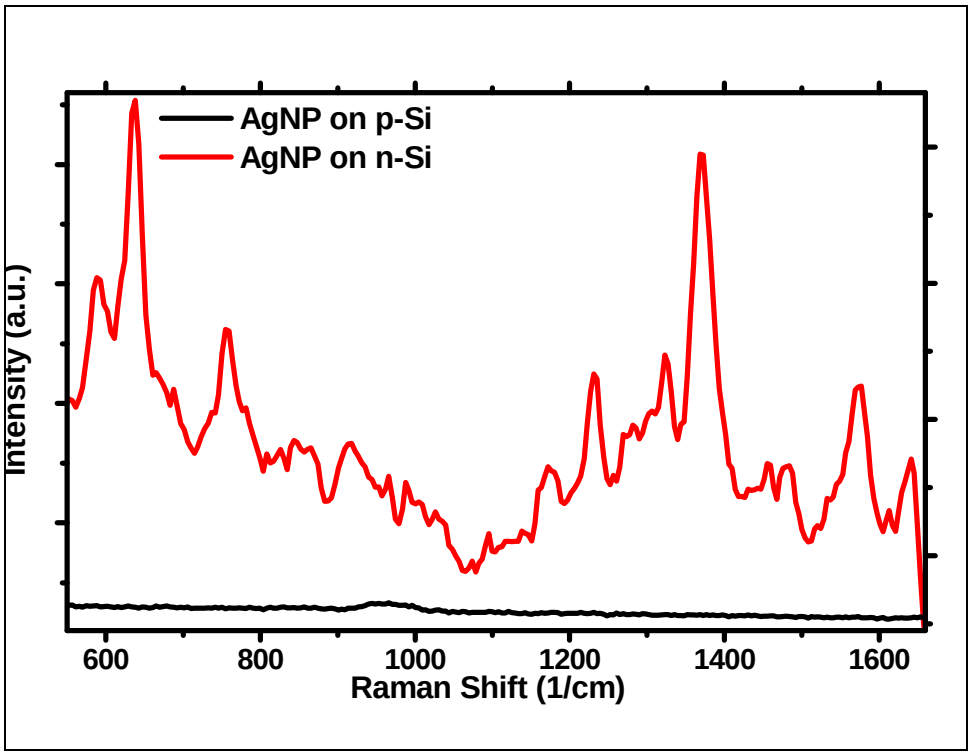

Figure 4.14. SERS spectra of 1 µl of acridine orange (1.3×10^{-6} M) spotted on p-type silicon (black) and n-type silicon (red).

Figure 4.14 displays the SERS spectra acquired from AO (1.3×10^{-6} M) spotted on negatively charged AgNP (black curve), and positively charged AgNP (red curve). When spotted on negatively charged AgNP, AO being positively charged binds more strongly on the surface of the AgNP, leading to the formation of distinct Raman peaks (red curve). However, when spotted on positively charged AgNP, due to Coulombic repulsion, there is lack of signal enhancement, accounting for no peaks at all (black curve).

IV.5) Impact of NP charging: Charge-Selective Fluorescence Quenching

To further elucidate the charging of the AgNP, confocal laser scanning microscopy of charged fluorophores spotted on charged AgNP was performed. Under the influence of incident electromagnetic radiation, the electrons of the fluorophore molecules undergo transitions to higher energy states. When the electrons return to their original states (i.e., after ns), the excess energy can be re-emitted (from the absorption event) in the form of photons which, thus resulting in fluorescence. However, the lifetime and quantum yield of the fluorescence is influenced by two primary factors; 1) radiative decay due to photon emission and 2) non-radiative decay due to energy dissipation to the surrounding environment. The fluorescing properties of molecular fluorophores in close proximity to metal NP are affected due to the strong electromagnetic field generated around the surface of the metal NP. Fluorophores that are very close to surface of the metal nanoparticle (i.e., < 5 nm) may interact electronically with the NP to donate the excited electrons to the metal, thus quenching the fluorescence by non-radiative channels available in the metal nanoparticle[61-65]. On the other hand, when there is no electron transfer, two opposite events can occur. Either fluorescence quenching takes place due to radiative energy (i.e., photon) transfer to the NP from the fluorophore. In this case, the photon energy is dissipated into heat in the metal through conduction electron collisions. Or, enhancement in fluorescence will be observed in the absence of radiative energy transfer due to enhanced near field distributions in the vicinity of the particle surface.

Figure 4.15 (a) shows a confocal microscopy image of 1 µl aliquots of fluorescein (1×10^{-7} M) spotted on positively charged AgNP. As mentioned previously, being negatively charged, F molecules get attracted to positively charged AgNP, resulting in an increased adsorption of F molecules on the surface of the AgNP, which causes the fluorescence to be quenched due the non-radiative electron transfer between F molecules and the AgNP. In Figure 4.15 (b) however, it can be observed that when 1 µl aliquot of fluorescein (1×10^{-7} M) was spotted on AgNP deposited on n-type Si, like charges between negatively charged F and AgNP cause the repellence of F molecules, increasing the concentration of F molecules in solution, leading to increased fluorescence.

To further elucidate the impact of NP charge on fluorescence quenching, a positively charged fluorophore, rhodamine-6G (R6G) was also employed. In the case of positively charged AgNP, the R6G molecules get repelled away from the AgNP, leading to an increase in the concentration of freely suspended R6G molecules in solution, resulting in the high fluorescence as seen in Figure 4.15 (c). On the contrary, when R6G is spotted on negatively charged AgNP, the dissimilar charges between the AgNP and the R6G molecules cause the R6G molecules to get adsorbed on the surface of the AgNP, resulting in quenching of the fluorescence (Figure 4.15 (d)).

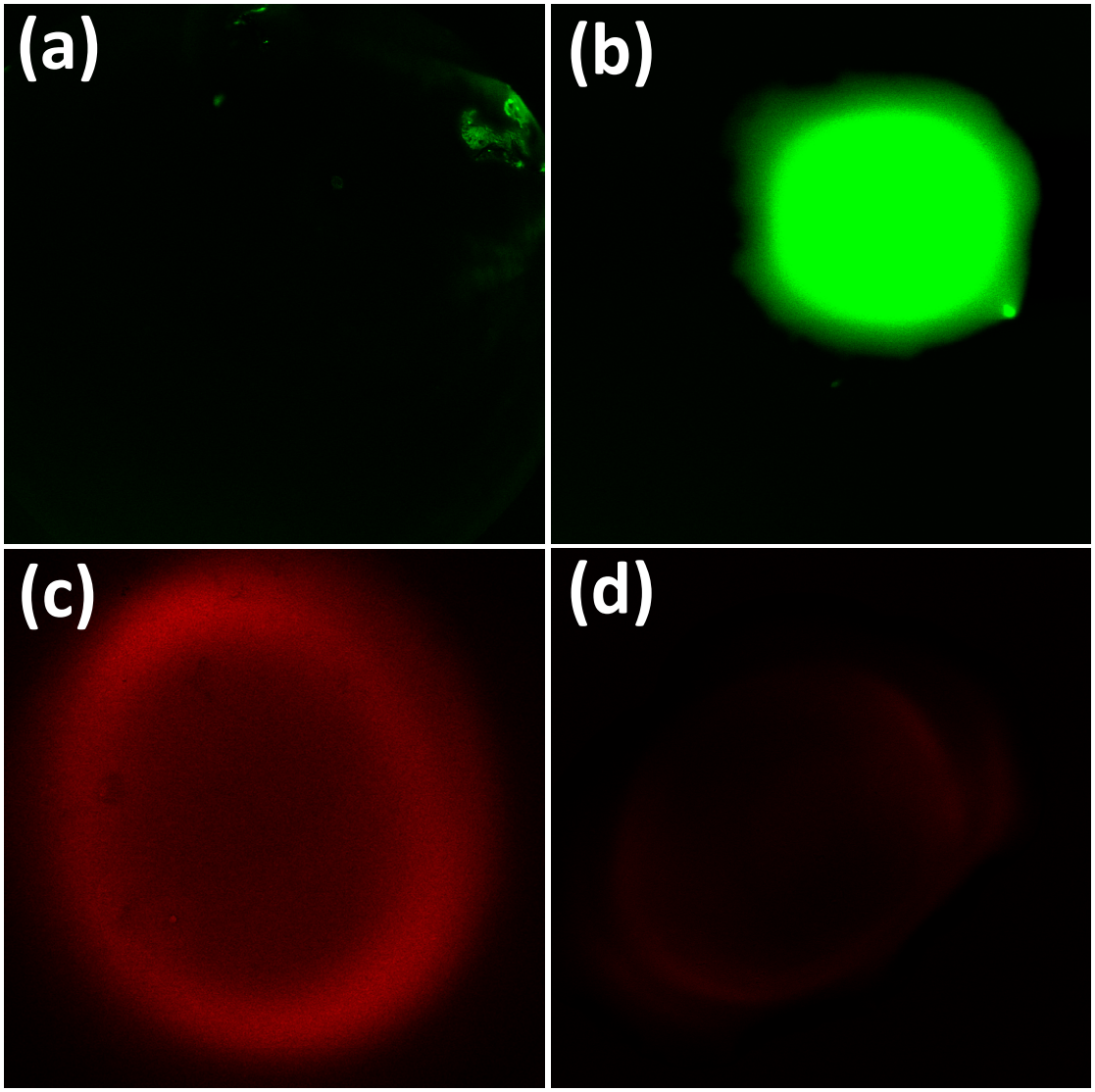

Figure 4.15. Confocal microscopy images of 1 µl of fluorescein (1×10^{-7} M) spotted on AgNP deposited on **(a)** p-type Si and **(b)** n-type Si and 1 µl of rhodamine 6G (1×10^{-8} M) spotted on **(c)** p-type Si **(d)** n-type Si.

The schematic of R6G molecules getting attracted to negatively charged AgNP and repelled away from positively charged AgNP is illustrated in Figures 4.16 and 4.17.

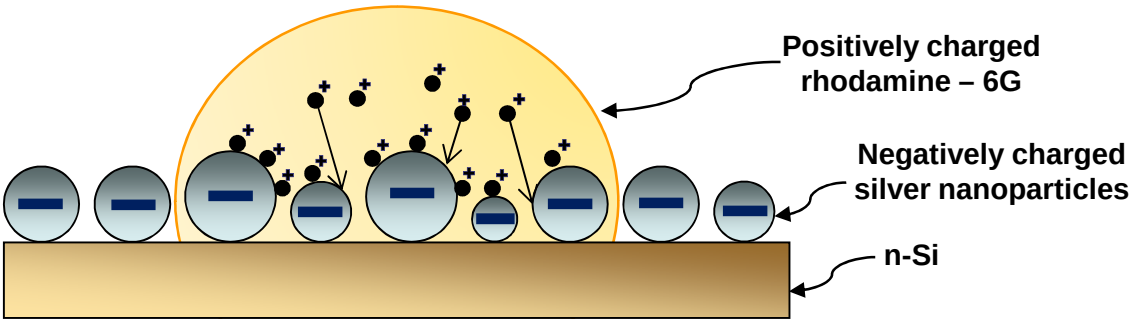

Figure 4.16. Schematic of rhodamine-6G molecules getting attracted to negatively charged AgNP.

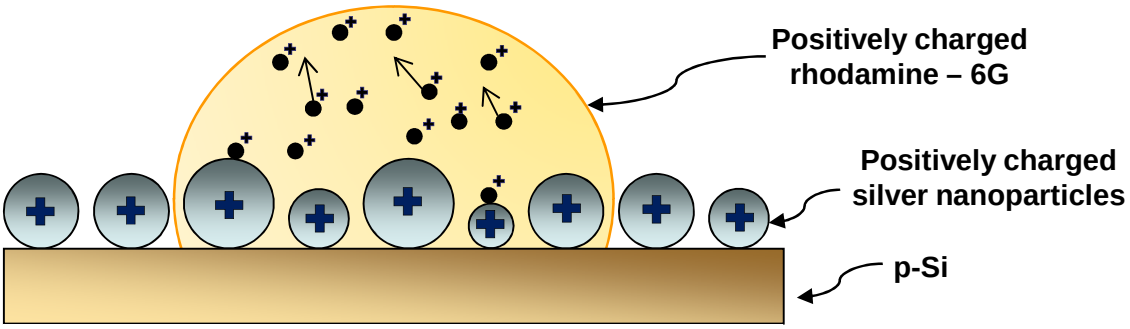

Figure 4.17. Schematic of rhodamine-6G molecules getting repelled away from positively charged AgNP.

CHAPTER V

CONCLUSIONS

V.1) Conclusions

Based on the results obtained in this thesis, the following conclusions are drawn:

1. Surfactant-free silver nanoparticles synthesized on semiconductor substrates (p-type and n-type Si) display charging, which is induced by the Fermi level difference. This charging can successfully be characterized by EFM.
2. As confirmed by EFM, the magnitude and polarity of NP charging can be controlled by varying the Fermi level difference between the metal and semiconductor.
3. It is established from AFM, optical extinction, and Mie scattering that the positively charged AgNP do not coalesce during electroless reduction despite a few nm interparticle spacing. In other words, the growth is self-inhibiting. As a result, strong electromagnetic interaction develops in between AgNP. Equivalently, plasmon hybridization occurs between the AgNP, identified by a well-resolved optical extinction peak. In contrast,

self-inhibiting growth is not observed for the negatively charged AgNP, resulting in coalescence. We explain these findings by an electrochemical model. As a positively-charged AgNP grows, the increasing electric potential on its surface leads to two consequences. First, the $[Ag^+]$ in the vicinity of the AgNP is reduced due to Coulombic repulsion. By Nernst's Equation, this reduction in $[Ag^+]$ results in decrease of the reduction potential of the reaction $Ag^+ + e^- \rightarrow Ag$. Second, the voltage (electric potential) on the AgNP increases and starts to compete with the above reaction for the reducing electron. When the reduction potential and nanoparticle voltage coincide, the net reduction stops. These effects are expected to be pronounced at the clearance between the neighboring AgNP where the electric potential is maximized due to superposition. Therefore, the self-inhibition of growth ultimately occurs, when the interparticle separation narrows down to a few nm, if not earlier. On the other hand, with growing negatively-charged AgNP, everything proceeds in the opposite direction. The reduction potential increases while the nanoparticle voltage decreases. Hence, the two competing impetus never coincide and counterbalance each other. As a result, the reduction reaction never stops until coalescence.

4. The practical conclusion, which draws from (3) is that only positively-charged metal nanoparticles reduced on a semiconductor (i.e., when the Fermi level of the metal is higher than that of the semiconductor) display localized surface plasmon resonance, and can be used as SPR sensors /

SERS substrates. Again, this conclusion is drawn for the electroless reduction.

5. The charged and surfactant-free AgNP serve as charge-selective SERS substrates for ions as demonstrated for fluorescein (-) and acridine orange (+). SERS is not detectable if the analyte and the AgNP charge are both positive or both negative. We attribute the absence of SERS signal to Coulombic repulsion between the nanoparticles and the analyte keeping the analyte off the near field regions around the nanoparticle associated with high SERS gains. In contrast, high signal to noise SERS signal is obtained when the AgNP and the analyte are oppositely charged. In this case, Coulombic attraction ensures adsorption of the analyte molecule on the NP surface and its excitation by the intense near fields.
6. Charged metal NP also account for charge-selective fluorescence quenching of ionic fluorophores (e.g., fluorescein (-), and rhodamine-6G (+)). Owing to Coulombic attraction, fluorescence quenching is only observed for oppositely charged AgNP and fluorophores.

V.2) Future Work

The mathematical analysis described in Section IV.2 is a simple one dimensional model that tries to explain the variation of the electric potential of a charged NP as a function of its size. The equation that accurately governs the electric potential distribution is given by

$$-\nabla^2\phi = \frac{\rho}{\varepsilon}$$

where,

ϕ is the potential,

ρ is the charge density

ε is the permittivity

This equation must be solved through the whole space-charge region including both, the semiconductor, and the metal. The charge density in the semiconductor and the metal can still be regarded as eN_D and zero respectively. The solution obtained by applying the relevant boundary conditions and using appropriate numerical methods would reveal a better understanding of the effect of NP size on its charge and electric field distribution.

REFERENCES

1. Liz-Marzán, L. M., Nanometals: Formation and color. *Materials Today* **2004,** *7* (2), 26-31.

2. Mie, G., Beiträge zur Optik trüber Medien speziell kolloidaler Goldlösungen. *Annals of Physics* **1908,** *25*, 377–445.

3. Horvath, H., Gustav Mie and the scattering and absorption of light by particles: Historic developments and basics. *Journal of Quantitative Spectroscopy and Radiative Transfer* **2009,** *110* (11), 787-799.

4. Haes, A. J.; Hall, W. P.; Chang, L.; Klein, W. L.; Van Duyne, R. P., A Localized Surface Plasmon Resonance Biosensor: First Steps toward an Assay for Alzheimer's Disease. *Nano Letters* **2004,** *4* (6), 1029-1034.

5. Haes, A. J.; Zou, S.; Schatz, G. C.; Van Duyne, R. P., Nanoscale Optical Biosensor: Short Range Distance Dependence of the Localized Surface Plasmon Resonance of Noble Metal Nanoparticles. *The Journal of Physical Chemistry B* **2004,** *108* (22), 6961-6968.

6. Yonzon, C. R.; Jeoung, E.; Zou, S.; Schatz, G. C.; Mrksich, M.; Van Duyne, R. P., A Comparative Analysis of Localized and Propagating Surface Plasmon Resonance Sensors: The Binding of Concanavalin A to a Monosaccharide Functionalized Self-Assembled Monolayer. *Journal of the American Chemical Society* **2004,** *126* (39), 12669-12676.

7. Kalkan, A. K.; Fonash, S. J., Laser-activated surface-enhanced Raman scattering substrates capable of single molecule detection. *Applied Physics Letters* **2006,** *89* (23), 233103-3.

8. Singhal, K.; Kalkan, A. K., Surface-Enhanced Raman Scattering Captures Conformational Changes of Single Photoactive Yellow Protein Molecules under Photoexcitation. *Journal of the American Chemical Society* **2009**.

9. Derkacs, D.; Lim, S. H.; Matheu, P.; Mar, W.; Yu, E. T., Improved performance of amorphous silicon solar cells via scattering from surface plasmon polaritons in nearby metallic nanoparticles. *Applied Physics Letters* **2006,** *89* (9), 093103.

10. Mirin, N. A.; Halas, N. J., Light-Bending Nanoparticles. *Nano Letters* **2009,** *9* (3), 1255-1259.

11. Nomura, W.; Ohtsu, M.; Yatsui, T., Nanodot coupler with a surface plasmon polariton condenser for optical far/near-field conversion. *Applied Physics Letters* **2005,** *86* (18), 181108.

12. Alvarez-Puebla, R. A.; Arceo, E.; Goulet, P. J. G.; Garrido, J. J.; Aroca, R. F., Role of Nanoparticle Surface Charge in Surface-Enhanced Raman Scattering. *The Journal of Physical Chemistry B* **2005,** *109* (9), 3787-3792.

13. Li, M.; Schnablegger, H.; Mann, S., Coupled synthesis and self-assembly of nanoparticles to give structures with controlled organization. *Nature* **1999,** *402* (6760), 393-395.

14. Sibbald, M. S.; Chumanov, G.; Cotton, T. M., Reductive properties of iodide-modified silver nanoparticles. *Journal of Electroanalytical Chemistry* **1997,** *438* (1-2), 179-185.

15. Mafune, F.; Kohno, J.-y.; Takeda, Y.; Kondow, T.; Sawabe, H., Structure and Stability of Silver Nanoparticles in Aqueous Solution Produced by Laser Ablation. *The Journal of Physical Chemistry B* **2000,** *104* (35), 8333-8337.

16. McConnell, W. P.; Novak, J. P.; Brousseau, L. C.; Fuierer, R. R.; Tenent, R. C.; Feldheim, D. L., Electronic and Optical Properties of Chemically Modified Metal Nanoparticles and Molecularly Bridged Nanoparticle Arrays. *The Journal of Physical Chemistry B* **2000,** *104* (38), 8925-8930.

17. Usui, H.; Shimizu, Y.; Sasaki, T.; Koshizaki, N., Photoluminescence of ZnO Nanoparticles Prepared by Laser Ablation in Different Surfactant Solutions. *The Journal of Physical Chemistry B* **2004,** *109* (1), 120-124.

18. Kalkan, A. K.; Fonash, S. J., Electroless Synthesis of Ag Nanoparticles on Deposited Nanostructured Si Films. *The Journal of Physical Chemistry B* **2005,** *109* (44), 20779-20785.

19. Horimoto, N.; Ishikawa, N.; Nakajima, A., Preparation of a SERS substrate using vacuum-synthesized silver nanoparticles. *Chemical Physics Letters* **2005,** *413* (1-3), 78-83.

20. Roark, S. E.; Rowlen, K. L., Thin silver films: influence of substrate and postdeposition treatment on morphology and optical properties. *Analytical Chemistry* **2002,** *66* (2), 261-270.

21. Schlegel, V. L.; Cotton, T. M., Silver-island films as substrates for enhanced Raman scattering: effect of deposition rate on intensity. *Analytical Chemistry* **2002,** *63* (3), 241-247.

22. Semin, D. J.; Rowlen, K. L., Influence of vapor deposition parameters on SERS active Ag film morphology and optical properties. *Analytical Chemistry* **2002,** *66* (23), 4324-4331.

23. Brandl, D. W.; Oubre, C.; Nordlander, P., Plasmon hybridization in nanoshell dimers. *The Journal of Chemical Physics* **2005,** *123* (2), 024701.

24. Elghanian, R.; Storhoff, J. J.; Mucic, R. C.; Letsinger, R. L.; Mirkin, C. A., Selective Colorimetric Detection of Polynucleotides Based on the Distance-Dependent Optical Properties of Gold Nanoparticles. *Science* **1997,** *277* (5329), 1078-1081.

25. Haynes, C. L.; Van Duyne, R. P., Nanosphere Lithography: A Versatile Nanofabrication Tool for Studies of Size-Dependent Nanoparticle Optics. *The Journal of Physical Chemistry B* **2001,** *105* (24), 5599-5611.

26. Haes, A. J.; Van Duyne, R. P., A Nanoscale Optical Biosensor: Sensitivity and Selectivity of an Approach Based on the Localized Surface Plasmon Resonance Spectroscopy of Triangular Silver Nanoparticles. *Journal of the American Chemical Society* **2002,** *124* (35), 10596-10604.

27. El-Sayed, I. H.; Huang, X.; El-Sayed, M. A., Surface Plasmon Resonance Scattering and Absorption of anti-EGFR Antibody Conjugated Gold Nanoparticles in Cancer Diagnostics: Applications in Oral Cancer. *Nano Letters* **2005,** *5* (5), 829-834.

28. Maier, S. A., Plasmonics: Fundamentals and Applications, Maier. **2007**.

29. Kneipp, K.; Kneipp, H.; Itzkan, I.; Dasari, R. R.; Feld, M. S., Ultrasensitive Chemical Analysis by Raman Spectroscopy. *Chemical Reviews* **1999,** *99* (10), 2957-2976.

30. Fleischmann, M.; Hendra, P. J.; McQuillan, A. J., Raman spectra of pyridine adsorbed at a silver electrode. *Chemical Physics Letters* **1974,** *26* (2), 163-166.

31. Jeanmaire, D. L.; Van Duyne, R. P., Surface raman spectroelectrochemistry: Part I. Heterocyclic, aromatic, and aliphatic amines adsorbed on the anodized silver electrode. *Journal of Electroanalytical Chemistry* **1977,** *84* (1), 1-20.

32. Xu, H.; Käll, M., Surface-Plasmon-Enhanced Optical Forces in Silver Nanoaggregates. *Physical Review Letters* **2002,** *89* (24), 246802.

33. Jackson, J. B.; Westcott, S. L.; Hirsch, L. R.; West, J. L.; Halas, N. J., Controlling the surface enhanced Raman effect via the nanoshell geometry. *Applied Physics Letters* **2003,** *82* (2), 257-259.

34. Nikoobakht, B.; El-Sayed, M. A., Surface-Enhanced Raman Scattering Studies on Aggregated Gold Nanorodsâ€ *The Journal of Physical Chemistry A* **2003,** *107* (18), 3372-3378.

35. Schwartzberg, A. M.; Grant, C. D.; Wolcott, A.; Talley, C. E.; Huser, T. R.; Bogomolni, R.; Zhang, J. Z., Unique Gold Nanoparticle Aggregates as a Highly Active Surface-Enhanced Raman Scattering Substrate. *The Journal of Physical Chemistry B* **2004,** *108* (50), 19191-19197.

36. Morrow, B. J.; Matijevic, E.; Goia, D. V., Preparation and stabilization of monodisperse colloidal gold by reduction with aminodextran. *Journal of Colloid and Interface Science* **2009,** *335* (1), 62-69.

37. Sondi, I.; Goia, D. V.; Matijevic, E., Preparation of highly concentrated stable dispersions of uniform silver nanoparticles. *Journal of Colloid and Interface Science* **2003,** *260* (1), 75-81.

38. Suber, L.; Sondi, I.; Matijevic, E.; Goia, D. V., Preparation and the mechanisms of formation of silver particles of different morphologies in homogeneous solutions. *Journal of Colloid and Interface Science* **2005,** *288* (2), 489-495.

39. Kahl, M.; Voges, E.; Kostrewa, S.; Viets, C.; Hill, W., Periodically structured metallic substrates for SERS. *Sensors and Actuators B: Chemical* **1998,** *51* (1-3), 285-291.

40. Zoval, J. V.; Biernacki, P. R.; Penner, R. M., Implementation of Electrochemically Synthesized Silver Nanocrystallites for the Preferential SERS Enhancement of Defect Modes on Thermally Etched Graphite Surfaces. *Analytical Chemistry* **1996,** *68* (9), 1585-1592.

41. Bjerneld, E. J.; Svedberg, F.; Kall, M., Laser-Induced Growth and Deposition of Noble-Metal Nanoparticles for Surface-Enhanced Raman Scattering. *Nano Letters* **2003,** *3* (5), 593-596

42. Prochazka, M.; Mojzes, P.; Stepanek, J.; VlcÌŒkova, B.; Turpin, P.-Y., Probing Applications of Laser-Ablated Ag Colloids in SERS Spectroscopy: Improvement of Ablation Procedure and SERS Spectral Testing. *Analytical Chemistry* **1997,** *69* (24), 5103-5108.

43. Sze, S. M., Physics of Semiconductor Devices, p. 371, **1969**.

44. Mélin, T.; Diesinger, H.; Deresmes, D.; Stiévenard, D., Electric force microscopy of individually charged nanoparticles on conductors: An analytical model for quantitative charge imaging. *Physical Review B* **2004,** *69* (3), 035321.

45. Nyffenegger, R. M.; Penner, R. M.; Schierle, R., Electrostatic force microscopy of silver nanocrystals with nanometer-scale resolution. *Applied Physics Letters* **1997,** *71* (13), 1878-1880.

46. Qiu, X. H.; Qi, G. C.; Yang, Y. L.; Wang, C., Electrostatic characteristics of nanostructures investigated using electric force microscopy. *Journal of Solid State Chemistry* **2008,** *181* (7), 1670-1677.

47. Terris, B. D.; Stern, J. E.; Rugar, D.; Mamin, H. J., Contact electrification using force microscopy. *Physical Review Letters* **1989,** *63* (24), 2669.

48. Yang, J.; Kim, J.; Lee, J.; Min, S.; Kim, H.; Wang, K. L.; Hong, J., Electrostatic force microscopy measurements of charge trapping behavior of Au nanoparticles embedded in metal-insulator-semiconductor structure. *Ultramicroscopy* **2008,** *108* (10), 1215-1219.

49. Belaidi, S.; Girard, P.; Leveque, G., Electrostatic forces acting on the tip in atomic force microscopy: Modelization and comparison with analytic expressions. *Journal of Applied Physics* **1997,** *81* (3), 1023-1030.

50. Lambert, J.; Guthmann, C.; Saint-Jean, M., Relationship between charge distribution and its image by electrostatic force microscopy. *Journal of Applied Physics* **2003,** *93* (9), 5369-5376.

51. Kimura, K.; Kobayashi, K.; Yamada, H.; Matsushige, K., Two-dimensional dopant profiling by scanning capacitance force microscopy. *Applied Surface Science* **2003,** *210* (1-2), 93-98.

52. Marchi, F.; Dianoux, R.; Smilde, H. J. H.; Mur, P.; Comin, F.; Chevrier, J., Characterisation of trapped electric charge carriers behaviour at nanometer scale by electrostatic force microscopy. *Journal of Electrostatics* **2008,** *66* (9-10), 538-547.

53. Boer, E. A.; Bell, L. D.; Brongersma, M. L.; Atwater, H. A.; Ostraat, M. L.; Flagan, R. C., Charging of single Si nanocrystals by atomic force microscopy. *Applied Physics Letters* **2001,** *78* (20), 3133-3135.

54. Ng, C. Y.; Chen, T. P.; Lau, H. W.; Liu, Y.; Tse, M. S.; Tan, O. K.; Lim, V. S. W., Visualizing charge transport in silicon nanocrystals embedded in SiO[sub 2] films with electrostatic force microscopy. *Applied Physics Letters* **2004,** *85* (14),

2941-2943.

55. Schaadt, D. M.; Yu, E. T.; Sankar, S.; Berkowitz, A. E., Charge storage in Co nanoclusters embedded in SiO[sub 2] by scanning force microscopy. *Applied Physics Letters* **1999,** *74* (3), 472-474.

56. Makov, G.; Nitzan, A.; Brus, L. E., On the ionization potential of small metal and dielectric particles. *The Journal of Chemical Physics* **1988,** *88* (8), 5076-5085.

57. Wood, D. M., Classical Size Dependence of the Work Function of Small Metallic Spheres. *Physical Review Letters* **1981,** *46* (11), 749.

58. Riviere, J. C., THE WORK FUNCTION OF GOLD. *Applied Physics Letters* **1966,** *8* (7), 172.

59. Kompan, M.; Novak, I.; Kulik, V., Spectra of second-order Raman scattering in porous silicon. *Journal of Experimental and Theoretical Physics* **2002,** *94* (4), 739-744.

60. Zimmerman, F.; Hossenfelder, B.; Panitz, J. C.; Wokaun, A., SERRS study of Acridine Orange and Its Binding to DNA Strands. *The Journal of Physical Chemistry* **2002,** *98* (48), 12796-12804.

61. Anger, P.; Bharadwaj, P.; Novotny, L., Enhancement and Quenching of Single-Molecule Fluorescence. *Physical Review Letters* **2006,** *96* (11), 113002-4.

62. Lakowicz, J.; Geddes, C.; Gryczynski, I.; Malicka, J.; Gryczynski, Z.; Aslan, K.; Lukomska, J.; Matveeva, E.; Zhang, J.; Badugu, R.; Huang, J., Advances in Surface-Enhanced Fluorescence. *Journal of Fluorescence* **2004,** *14* (4), 425-441.

63. Dulkeith, E.; Ringler, M.; Klar, T. A.; Feldmann, J.; Munoz Javier, A.; Parak, W. J., Gold Nanoparticles Quench Fluorescence by Phase Induced Radiative Rate Suppression. *Nano Letters* **2005,** *5* (4), 585-589.

64. Trabesinger, W.; Kramer, A.; Kreiter, M.; Hecht, B.; Wild, U. P., Single-molecule near-field optical energy transfer microscopy. *Applied Physics Letters* **2002,** *81* (11), 2118-2120.

65. Thomas, K. G.; Kamat, P. V., Chromophore-Functionalized Gold Nanoparticles. *Accounts of Chemical Research* **2003,** *36* (12), 888-898.

VITA

Karthik Shankar Bhatt

Candidate for the Degree of

Master of Science

Thesis: CHARGE-SELECTIVE RAMAN SCATTERING AND FLUORESCENCE QUENCHING BY "NANO-METAL ON SEMICONDUCTOR" SUBSTRATES

Major Field: Mechanical Engineering

Biographical:

Personal Data: Born on September 8th 1983 in Shimoga, Karnataka, India

Education:

2007 – 2009: Oklahoma State University, Stillwater, Oklahoma
Master of Science in Mechanical Engineering

2001 – 2005: Visvesvaraya Technological University, Belgaum, India
Bachelor of Engineering in Mechanical Engineering

1999 – 2001: Kumarans Pre-University College, Bangalore, India

Experience:

Research Assistant, Functional Nanomaterials Laboratory, OSU
Jan 2007 – Dec 2009
Teaching Assistant, Mechanical and Aerospace Engineering, OSU
Jan 2007 – May 2009
Research Assistant, Indian Institute of Science, Bangalore, India
Jun 2006 – Dec 2006
Requirements Analyst – Etheract Software Labs, Bangalore, India
July 2005 – Mar 2006

Name: Karthik Shankar Bhatt Date of Degree: May, 2010

Institution: Oklahoma State University Location: Stillwater, Oklahoma

Title of Study: CHARGE-SELECTIVE RAMAN SCATTERING AND FLUORESCENCE QUENCHING BY "NANO-METAL ON SEMICONDUCTOR" SUBSTRATES

Pages in Study: 55 Candidate for the Degree of Master of Science

Major Field: Mechanical Engineering

Scope and Method of Study:
An interesting attribute of monolayers of metal nanoparticles (NP) synthesized on semiconductor substrates is charging of NP induced by Fermi level difference. In this study, silver nanoparticles (AgNP) were synthesized on high conductivity Si wafers (p- and n-Si) employing the electroless reduction of $AgNO_3$ by Si, as well as vapor deposition. Electric force microscopy (EFM) confirms the presence of NP charge and its expected variation (polarity and magnitude) with the Fermi level difference. Furthermore, Atomic force microscopy (AFM), optical absorption, and Mie scattering was performed to study the impact of this charging phenomenon on self-inhibiting growth and coalescence of AgNP during chemical reduction. The present work demonstrates that this selective charging of the AgNP can be exploited in charge-selective Raman scattering and fluorescence quenching of ionic fluorophores (fluorescein (-), rhodamine-6G (+) and acridine orange (+)).

Findings and Conclusions:
Owing to Fermi level differences, AgNP synthesized on p-Si acquire a positive charge, while AgNP synthesized on n-Si acquire a negative charge. The polarity and magnitude of the acquired charge can be controlled by varying the Fermi level difference. Owing to the selective charging, during electroless deposition, positively charged AgNP display self-inhibiting growth and do not coalesce despite a few nm interparticle spacing, leading to strong electromagnetic interactions between the AgNP. As a result, well resolved hybrid plasmon modes develop, enabling the use of positively charged AgNP as SPR sensors / SERS substrates. In contrast, self-inhibition is not observed for negatively charged AgNP, due to which the nanoparticles coalesce, resulting in the loss of LSPR. Charged AgNP can be utilized as charge-selective SERS substrates for ionic analytes. Due to Coulombic interactions between the charged AgNP and ionic fluorophores, SERS is only observed when the analyte and the AgNP are oppositely charged. Charged metal NP also display charge-selective fluorescence quenching of ionic fluorophores. Again, owing to Coulombic interactions, fluorescence quenching is only observed for oppositely charged metal NP and fluorophores.

ADVISER'S APPROVAL: Dr. A. Kaan Kalkan